scientific reports

Check for updates

OPEN

Finite element analysis predicts Ca²⁺ microdomains within tubular-sarcoplasmic reticular junctions of amphibian skeletal muscle

Oliver J. Bardsley[1], Hugh R. Matthews[1] & Christopher L.-H. Huang[1,2]✉

A finite element analysis modelled diffusional generation of steady-state Ca²⁺ microdomains within skeletal muscle transverse (T)-tubular-sarcoplasmic reticular (SR) junctions, sites of ryanodine receptor (RyR)-mediated SR Ca²⁺ release. It used established quantifications of sarcomere and T-SR anatomy (radial diameter $d = 220$ nm; axial distance $w = 12$ nm). Its boundary SR Ca²⁺ influx densities, J_{influx}, reflected step impositions of *influxes*, $\Phi_{influx} = J_{influx}\left(\frac{\pi d^2}{4}\right)$, deduced from previously measured Ca²⁺ signals following muscle fibre depolarization. *Predicted* steady-state T-SR junctional edge [Ca²⁺], [Ca²⁺]$_{edge}$, matched reported corresponding *experimental* cytosolic [Ca²⁺] elevations given diffusional boundary *efflux* $\Phi_{efflux} = \frac{D[Ca^{2+}]_{edge}}{\lambda}(\pi dw)$, established cytosolic Ca²⁺ diffusion coefficients ($D = 4 \times 10^7$ nm²/s) and exit length $\lambda = 9.2$ nm. Dependences of *predicted* [Ca²⁺]$_{edge}$ upon J_{influx} then matched those of *experimental* [Ca²⁺] upon Ca²⁺ release through their entire test voltage range. The resulting model consistently predicted elevated steady-state T-SR junctional ~ μM-[Ca²⁺] elevations radially declining from maxima at the T-SR junction centre along the entire axial T-SR distance. These [Ca²⁺] heterogeneities persisted through 10⁴- and fivefold, variations in D and w around, and fivefold reductions in d below, control values, and through reported resting muscle cytosolic [Ca²⁺] values, whilst preserving the flux conservation ($\Phi_{influx} = \Phi_{efflux}$) condition, $[Ca^{2+}]_{edge} = \frac{\lambda d J_{influx}}{4Dw}$. Skeletal muscle thus potentially forms physiologically significant ~ μM-[Ca²⁺] T-SR microdomains that could regulate cytosolic and membrane signalling molecules including calmodulin and RyR, These findings directly fulfil recent experimental predictions invoking such Ca²⁺ microdomains in observed regulatory effects upon Na⁺ channel function, in a mechanism potentially occurring in similar restricted intracellular spaces in other cell types.

Intracellular endoplasmic or sarcoplasmic reticular (SR) membrane systems gating store Ca²⁺ release into the cytosol following surface membrane activation, often involving ryanodine receptor (RyR) activation, occur widely amongst cell types. These include both excitable (skeletal, cardiac and smooth muscle, and cerebellar Purkinje[1–3], hippocampal[4] and other central nervous system neurones[5,6]) and non-excitable, including thrombocyte, cell types[7,8]. These intracellular membranes often form appositions with surface membrane with proximities (< 10–30 nm) permitting direct protein–protein/lipid interaction[9,10] though not accommodating entire organelles. Their intervening electron-dense cytosol could also reflect local concentrations of proteins, lipids or ions. Electron microscopic sections can reveal parallel alignments extending over ~ 100–400 nm distances without fusion of the component membranes potentially offering restricted diffusion spaces permitting ion, including Ca²⁺, accumulation and microdomain formation.

In skeletal and cardiac muscle, following surface membrane propagation, Na⁺ channel mediated action potentials are conducted into the cellular interior at regular intervals along the muscle length through electrically continuous transverse (T-) tubular membranes. At specific regions, these come geometrically close (~ 12 nm) to, whilst remaining electrically isolated from, terminal cisternal membranes of the SR Ca²⁺ store. The resulting T-SR triad and dyad junctions are strategic to excitation–contraction coupling[11–13]. In cardiac muscle, tubular

¹Physiological Laboratory, University of Cambridge, Downing Street, Cambridge CB2 3EG, UK. ²Department of Biochemistry, University of Cambridge, Tennis Court Road, Cambridge CB2 1QW, UK. ✉email: clh11@cam.ac.uk

1

Name of variable	Definition	Value (physiological units)	Value (SI units)				
Geometrical characteristics: muscle fibre							
Length of sarcomere[41]	l	3.65 μm	3.65×10^{-6} m				
Diameter of fibre[39]	a	100 μm	1.00×10^{-4} m				
Surface membrane capacitance[39]	C_S	1.0 μF/cm²	1.00×10^{-2} F/m²				
T-Tubular membrane capacitance[40]	C_T	5.0 μF/cm²	5.00×10^{-2} F/m²				
Derived variables used in modelling							
Ratio of T-tubular to surface membrane capacitance	(C_T/C_S)	5.0	5.0				
Sarcomere surface membrane area	$A_S = \pi a l$	1147 μm²	1.147×10^{-9} m²				
Sarcomere tubular membrane area	$A_T = (C_T/C_S)\pi a l$	5733 μm²	5.733×10^{-9} m²				
Sarcomere volume	$V = \pi a^2 l/4$	2.87×10^4 μm³	2.87×10^{-14} m³				
Geometrical characteristics: T-SR junction							
Proportion of T-tubular membrane area apposed to triad junctions[44]	ξ	0.3	0.3				
Width of T-SR Junction[44]	w	12 nm	1.2×10^{-8} m				
Diameter of sarcoplasmic reticular (SR) terminal cisternae[42,43]	d	220 nm	2.20×10^{-7} m				
Derived variables used in modelling							
SR membrane area of T-SR junction	$\pi d^2/4$	38,013.27 nm²	3.8013×10^{-14} m²				
Area at edge of T-SR junction	$\pi d w$	8293.804 nm²	8.2938×10^{-14} m²				
Ratio of volume of T-SR spaces to that of whole cell	$\xi w A_T/V$	7.20×10^{-4}	7.20×10^{-4}				
Tubular membrane area abutted by T-SR junction	$A_{TSR} = \xi A_T$	1720 μm²	1.720×10^{-9} m²				
Total number of T-SR junctions in one sarcomere	$4A_{TSR}/(\pi d^2)$	4.5248×10^4	4.5248×10^4				
Total number of T-SR junctions in unit volume of muscle	$N_{TSR} = 16\xi C_T/(\pi d^2 a C_S)$	$1.5784 \times 10^{15}/$dm³	$1.5784 \times 10^{18}/$m³				
Flux properties, previous experimental results[45]							
Test membrane potential, E (mV)		−45	−40	−30	−20	−10	0
Maximum rate of [Ca²⁺] increase, d[Ca²⁺]/dt (μmol/(dm³s))		3.55	18.0	90.0	120.0	170.0	180.0
Peak cytosolic calcium concentration, [Ca²⁺]$_{max}$ (μmol/dm³)		0.135	0.511	1.711	2.427	2.858	3.161
Computed boundary conditions over range of varied test voltages: T-SR junction							
Ca²⁺ flux density into T-SR junction, J_{influx} (mol/(nm²s))		5.92×10^{-26}	3.00×10^{-25}	1.50×10^{-24}	2.00×10^{-24}	2.83×10^{-24}	3.00×10^{-24}
Ca²⁺ flux into T-SR junction, Φ_{influx} (mol/s)		2.25×10^{-21}	1.14×10^{-20}	5.70×10^{-20}	7.60×10^{-20}	1.07×10^{-19}	1.14×10^{-19}
Ca²⁺ diffusion coefficient in vivo[46,47], D (nm²/s)		4×10^7	4×10^7	4×10^7	4×10^7	4×10^7	4×10^7
Exit length, λ (nm)		9.2	9.2	9.2	9.2	9.2	9.2

Table 1. Structural characteristics of amphibian skeletal muscle fibres and transverse tubular-sarcoplasmic reticular (T-SR) junctions.

membrane Ca²⁺ influx through voltage-activated dihydropyridine receptors (DHPR2; Cav1.2) activates SR Ca²⁺ release by cardiac-type SR RyR2[14]. In skeletal muscle, Ca$_v$1.1 DHPR1 conformational changes themselves allosterically activate directly coupled RyR1[15].

Released Ca²⁺ then diffuses into the cytosol activating nearby myofilaments and consequent muscle contraction, prior to its SR Ca²⁺-ATPase mediated re-sequestration at longitudinal as opposed to T-SR membrane sites. However, recent evidence implicates Ca²⁺ in further regulatory functions involving T and SR membrane proteins. Skeletal and cardiac muscle Na⁺ channels (Na$_v$1.4 and Na$_v$1.5) possess potential Ca²⁺ and calmodulin (CaM) binding modulatory sites[16]. Here Ca²⁺ can bind directly to the Na$_v$ C-terminal domain at one or more of its EF-like hand motifs[17], or indirectly, through Ca²⁺/CaM binding, to its isoleucine-glutamine (IQ) domain region following initial Ca²⁺ binding to EF-hand motifs on CaM[18,19] or to a site between Na$_v$ domains III and IV[20]. Voltage-gated Na⁺ channels additionally contain sites phosphorylatable by Ca²⁺/CaM-regulated CaM kinase II (CaMKII)[21], and by protein kinase C[22]. In vitro single-cell patch clamp studies reported that elevating [Ca²⁺]$_i$ to ~2 μM by rapid Ca²⁺ photo-release or overspill from neighbouring Ca²⁺ channels, reduced Na⁺ current, I_{Na}, in Na$_v$1.4-transfected HEK293 cells and skeletal muscle cell lines. These effects were abrogated by intracellular BAPTA[23], or mutations involving either the CaM Ca²⁺-binding-EF hands or the Nav1.4 C-terminal IQ domain[19,23,24].

Intact native murine skeletal muscle fibres were also studied by a loose patch clamping technique that minimized perturbations in intracellular Ca²⁺ signalling[25]. Activation or inhibition of SR Ca²⁺ release then respectively

reduced or increased Na$^+$ current, I_{Na}. The latter were accomplished by direct pharmacological RyR1 activation by caffeine or 8-(4-chlorophenylthio)-2′-O-methyladenosine-3′,5′-cyclic monophosphate (8-CPT), or RyR1 inhibition by dantrolene. Dantrolene pretreatment further abrogated the downregulatory effects of caffeine or 8-CPT on I_{Na}[26,27]. Murine cardiac muscle showed similar effects when SR Ca^{2+} release was enhanced either by 8-CPT challenge, or with the RyR2-P2328S genetic modification[28,29]. In contrast, cyclopiazonic acid (CPA) increased skeletal muscle I_{Na}, while preserving its time courses, steady-state half-maximum voltages and steepness factors. CPA pre-treatment also abrogated the effects of caffeine[30]. Yet previous Ca^{2+} fluorescence studies performed in rat soleus and oesophageal striated muscle using fluo-3-AM and fura-PE3-AM had reported that both caffeine and CPA increased bulk cytosolic [Ca^{2+}][31–34]. However, in contrast to modifying RyR-mediated SR Ca^{2+} release, CPA inhibits SR Ca^{2+}-ATPase (SERCA)-mediated cytosolic Ca^{2+} re-uptake[31,32]. The consequent store Ca^{2+} depletion would then be expected to reduce, rather than increase, RyR1-mediated Ca^{2+} influx into the T-SR junction[30].

These paradoxical findings prompted suggestions that RyR1-mediated Ca^{2+} release took place into a microdomain in the vicinity of both the SR RyR1 and the T-tubular membrane Na$_v$1.4 and that the local elevation in Ca^{2+} concentration, [Ca^{2+}]$_{TSR}$, would then modify Na$_v$1.4 function[30]. Such a hypothesis would predict contrasting increases and decreases in local microdomain [Ca^{2+}] following caffeine, and dantrolene or CPA challenge. The narrow, ~ 12 nm T-SR junctions that could form spaces with restricted intracellular diffusion close to the RyR1 Ca^{2+}-release sites might be implicated in such microdomain formation. These could result in changes in local in vivo [Ca^{2+}]$_{TSR}$, distinct from those of [Ca^{2+}]$_i$ in the remaining bulk cytosol. This could explain the contrasting actions of RyR1 agonists and RyR1 or SERCA antagonists on I_{Na} through correspondingly contrasting effects on local Ca^{2+} or Ca^{2+}/CaM levels, to which the Na$_v$1.4 would be directly or indirectly exposed, despite their similar effects on bulk cytosolic [Ca^{2+}]$_i$[33,34].

Direct experimental explorations for such [Ca^{2+}]$_{TSR}$ microdomains possibly using fluorescent Ca^{2+} indicator methods need to address the small dimensions and dispersed nature of the T-SR compartment[35–37]. The present complementary approach applies diffusional modelling techniques[38] to explore the physical parameters permitting accumulation or depletion of released SR Ca^{2+} within the T-SR junction. It demonstrated that established anatomical and physiological features related to skeletal muscle excitation–contraction coupling are physically compatible with generation of significant Ca^{2+} microdomains in both activated and resting muscle fibres. We then discuss their possible physiological effects both in myocyte T-SR junctions and in similar membrane appositions in other cell types.

Results

T-SR junction structure represented using a formal geometric model.

We employed anatomical, optical and electron microscope quantifications of sarcomere and T-SR junction structure from amphibian twitch fibres as the muscle type for which the fullest data are available[39–44]. This provided the required details of T-tubular-sarcoplasmic reticular (T-SR) junction anatomy for the modelling studies (Table 1). First, the reported values of sarcomere length l, fibre diameter a, and relative tubular (T) to surface (S) membrane area reflected in the ratio of their respective capacitances C_T/C_S, yielded the sarcomeric surface membrane area:

$$A_S = \pi a l \tag{1}$$

and the total tubular membrane surface area:

$$A_T = \left(\frac{C_T}{C_S}\right)\pi a l \tag{2}$$

Morphometric electron micrographic estimates of the proportion ξ of the total tubular membrane area A_T accounted for by T-SR junctions[44] then gave the total T-tubular membrane area contributing to T-SR junction structures $A_{TSR} = \xi A_T$.,w,d of SR membrane enclosed in a single T-SR junction. The latter was accordingly modelled as a circularly symmetrical disk-shaped space of dimensions $w = 12$ nm and $d = 220$ nm (Fig. 1,

Ca^{2+} diffusion into and through a single T-SR junction modelled by finite element analysis.

The finite element analysis of steady state Ca^{2+} diffusion through a single T-SR space used the circular ends of the geometry defined above to represent its respective T-tubular and SR membranes. The rim separating their edges connected the T-SR and remaining intracellular spaces. *Influx* boundary conditions were supplied by a steady-state and uniform Ca^{2+} influx density J_{influx} across the SR membrane face of each individual T-SR junction:

$$\Phi_{influx} = J_{influx}\left(\frac{\pi d^2}{4}\right) \tag{3}$$

In contrast, the T-tubular face represented a zero-flux boundary surface. The Ca^{2+} then diffuses through and leaves the T-SR space at the rim with diffusion coefficient D:

$$\frac{\partial\left[Ca^{2+}\right]}{\partial t} - \nabla \cdot \left(D\nabla\left[Ca^{2+}\right]\right) + p\left[Ca^{2+}\right] = 0 \tag{4}$$

Away from the boundaries where $p = 0$:

$$\frac{\partial\left[Ca^{2+}\right]}{\partial t} = \nabla \cdot \left(D\nabla[Ca^{2+}]\right) \tag{5}$$

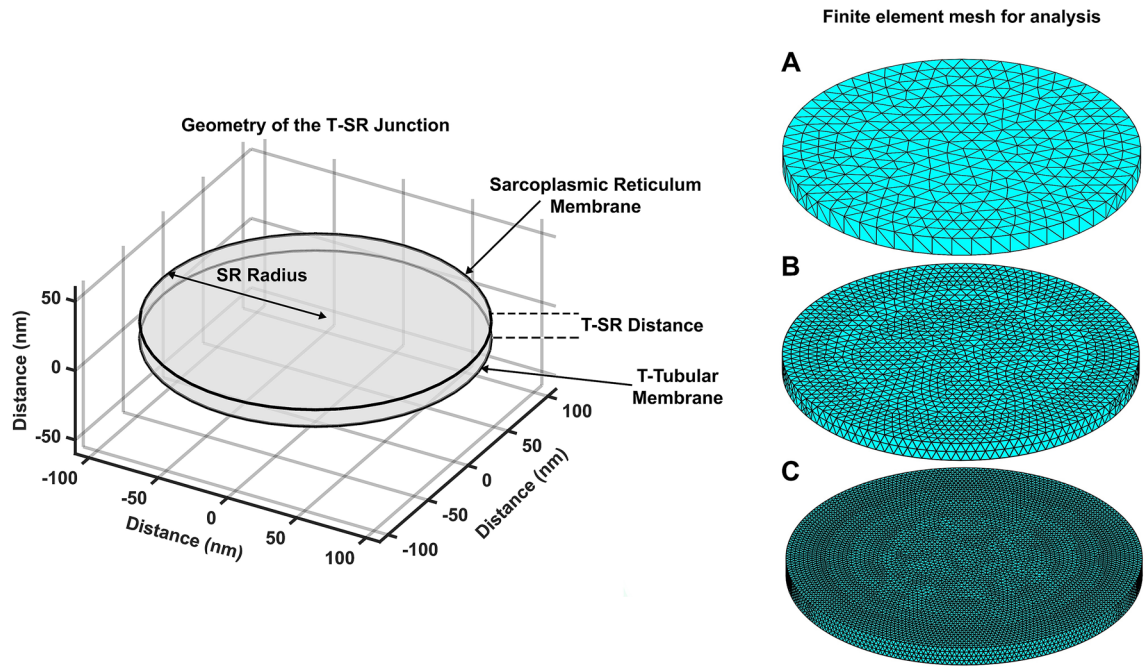**Finite element mesh for analysis**

Figure 1. T-SR junction structure represented using a formal geometric model divided into finite elements. Left: Geometrical representation of formalized T-SR junction represented as two disks, respectively of tubular (T) and sarcoplasmic reticular (SR) membranes, of diameter, $d = 220$ nm, within the radial (xy) plane, separated along an axial (z) direction by a T-SR distance, $w = 12$ nm. Right: Superimposition of finite elements dividing T-SR junction geometry into tetrahedral 'elements' with specified maximum lengths of (**A**) 12 nm, or 100%, (**B**) 6 nm or 50%, and (**C**) 3 nm or 25%, of the T-SR distance respectively. Reduced maximum tetrahedral lengths increase the number of elements, within which each time-dependent solution is generated, increasing spatial resolution in the solution concentration profile.

At the *efflux* boundary, the constant p is proportional to the diffusion coefficient D, $p = D/\lambda$, giving:

$$\frac{\partial \left[Ca^{2+} \right]}{\partial t} = \nabla \cdot \left(D\nabla[Ca^{2+}] \right) - \left(\frac{D}{\lambda} \right) \left[Ca^{2+} \right] = 0 \tag{6}$$

This edge region thus incorporates a first-order efflux Neumann BC describing diffusional Ca^{2+} efflux Φ_{efflux} leaving the T-SR space across its edge area πdw, giving efflux:

$$\Phi_{\text{efflux}} = J_{efflux}(\pi\, \mathrm{dw}) \tag{7}$$

Its efflux density J_{efflux} is proportional to the edge Ca^{2+} concentration $[Ca^{2+}]^{\text{TSR}}_{\text{edge}}$:

$$J_{\text{efflux}} = \frac{D\left[Ca^{2+} \right]_{\text{edge}}}{\lambda} \tag{8}$$

This gives efflux equation:

$$\Phi_{\text{efflux}} = \frac{D\left[Ca^{2+} \right]_{\text{edge}}}{\lambda}(\pi\, dw) \tag{9}$$

Its Fick's Law constant D/λ comprises the Ca^{2+} diffusion coefficient D and empirical exit length λ. The latter provides a geometrical parametrization of the re-uptake of the dissipated Ca^{2+} from a well stirred cytosolic compartment by SERCA activity without saturation. The λ term represents the only free parameter in the entire modelling analysis.

Diffusional processes within the T-SR junction were represented by superimposing a finite element mesh upon the T-SR junction geometry using PDE Toolbox, dividing that 3D geometry into fine tetrahedral elements of specified maximum length χ (Fig. 1, Right panels A–C). Different mesh sizes progressively divided the T-SR space into (A) 12 nm, (B) 6 nm and (C) 3 nm tetrahedral elements; finer mesh sizes were used where modelling investigated axial in addition to radial $[Ca^{2+}]$ gradients and in duplicate runs matching different mesh sizes to validate those used in the reconstructions. The FEM and MATLAB solved the equations specified for the system and specified input parameters producing a $[Ca^{2+}]$ dataset in the form of an array, whose spatial resolution was determined by the fineness of the mesh, set by the maximum element length χ. Its steady state solutions satisfied the overall conservation condition,

$$\Phi_{\text{influx}} = \Phi_{\text{efflux}} \tag{10}$$

between influx and efflux boundaries, yielding the condition (see Eqns. 3 and 9):

$$J_{\text{influx}} \left(\frac{\pi d^2}{4} \right) = \frac{D \left[\text{Ca}^{2+} \right]_{\text{edge}}}{\lambda} (\pi \, \text{dw}) \tag{11}$$

This condition was used in checks for the steady state condition in detailed explorations of the effect of specific parameters that follow.

Sarcoplasmic reticulum Ca²⁺ release producing Ca²⁺ microdomains characterized by radial concentration gradients in the T-SR junction.

The modelling process first sought three-dimensional (3D) reconstructions of radial steady state $[\text{Ca}^{2+}]$ distributions resulting from diffusional processes using the computational T-SR parameters listed in Table 1. Ca²⁺ release influx densities into each individual T-SR junction, J_{influx}, used in the MATLAB program PDE Toolbox, could be related to previously reported[45] experimental initial rates of SR Ca²⁺ release $d[\text{Ca}^{2+}]/dt$. The latter would give a Ca²⁺ flux into the sarcomere cytosolic volume V of $\left\{ \frac{d[\text{Ca}^{2+}]}{dt} \right\} V$ in turn corresponding to a flux density into each T-SR junction of:

$$J_{\text{influx}} = \frac{\left\{ \frac{d[\text{Ca}^{2+}]}{dt} \right\} V}{\xi A_T} \tag{12}$$

Antipyrylazo III absorbances in amphibian skeletal muscle fibres subject to voltage clamp steps from a − 90 mV resting to a 0 mV test membrane potential[45] reported a value of $d[\text{Ca}^{2+}]/dt = 180 \, \mu\text{mol}/(\text{dm}^3 \, \text{s})$. The Ca²⁺ then diffuses through the T-SR space down its resulting concentration gradients with the diffusion constant $D = 4.0 \times 10^7 \, \text{nm}^2/\text{s}$ previously reported for amphibian skeletal muscle[46–48]. The Ca²⁺ finally leaves the T-SR junction space effluxing into surrounding cytosol at the edge of the T-SR junction across diffusional area πdw at a rate driven by $[\text{Ca}^{2+}]^{\text{TSR}}_{\text{edge}}$. This proved close and proportional to reported experimental peak cytosolic Ca²⁺ concentration, $[\text{Ca}^{2+}]_{\text{max}}$ at the explored 0 mV test voltage with the use of an exit length value $\lambda = 9.2 \, \text{nm}$[45].

An overall rate constant describing the dependence of the summed Ca²⁺ fluxes upon $[\text{Ca}^{2+}]^{\text{TSR}}_{\text{edge}}$ could be determined using the predicted number of T-SR junctions in unit muscle volume,

$$N_{\text{TSR}} = \frac{16\xi \left(\frac{C_T}{C_S} \right)}{\pi a d^2} \tag{13}$$

The total Ca²⁺ efflux into unit muscle volume is then:

$$N_{\text{TSR}} \Phi_{\text{efflux}} = \frac{16 \xi w \left(\frac{C_T}{C_S} \right) D \left[Ca^{2+} \right]_{\text{edge}}}{\lambda a d} \tag{14}$$

The constant of proportionality describing this linear dependence on $[\text{Ca}^{2+}]^{\text{TSR}}_{\text{edge}}$ is then.

$$\frac{16\xi D w \left(\frac{C_T}{C_S} \right)}{\lambda a d} = 5.69 \, \text{s}^{-1}$$

This resulting rate constant is smaller than but comparable to experimental rate constants describing eventual SR resequestration of the released cytosolic Ca²⁺. Thus, previous experimental studies suggested rate constants for such unsaturable SR Ca²⁺-ATPase mediated Ca²⁺ uptake around $22.3 \pm 8.14/\text{s}$ under similarly steady state conditions where Ca²⁺ binding to remaining, saturable, fast-exchanging cytosolic binding sites was constant[49].

Figure 2A–C map the predicted $[\text{Ca}^{2+}]$ through the radial geometry of the T-SR junction. The false colour maps reconstruct perspective steady-state $[\text{Ca}^{2+}]$ at the (A) tubular and (B) SR membrane faces, and (C) en face $[\text{Ca}^{2+}]$ at the tubular membrane face of the T-SR junction. Between elements where a solution has not been calculated, the result is interpolated automatically according to the coarseness of the mesh. These maps show a significant $[\text{Ca}^{2+}]$ heterogeneity or microdomain across the radial axis resulting in a > fivefold difference between centre and edge T-SR junction $[\text{Ca}^{2+}]$. These resulting Ca²⁺ microdomains extended the entire T-SR distance mapping $[\text{Ca}^{2+}]$ gradients onto the tubular membrane surface. The colour map (Fig. 2D) shows a surface plot, with radial x and y axes representing the width and length of the T-tubular membrane abutted by SR and the axial z axis the $[\text{Ca}^{2+}]$ at that point, displaying $[\text{Ca}^{2+}]$ nonuniformities extending across the T-tubular membrane.

Figure 2E demonstrates an axially sliced Ca²⁺ microdomain extending to the edge of the T-SR junction with $[\text{Ca}^{2+}]$ radially falling ~ fivefold over ~ 100 nm from the T-SR junction centre. Figure 2F maps steady state $[\text{Ca}^{2+}]$ within a section taken along a midline axial plane through the T-SR junction. It illustrates diffusional effects following SR Ca²⁺ release along the bottom of the frame and the resulting nearly axially uniform $[\text{Ca}^{2+}]$ and radial $[\text{Ca}^{2+}]$ gradients running towards the T-SR junction edge.

Steady state microdomain [Ca²⁺] quantified with position within the T-SR junction.

The Ca²⁺ microdomain represented above was quantified from the array of $[\text{Ca}^{2+}]$ values at each element with time following imposition of the Ca²⁺ influx density J_{influx}; missing data between element solutions were interpolated from nearby nodal solutions. To quantify $[\text{Ca}^{2+}]$ with time in the microdomain, each finite element in the mesh

Figure 2. Sarcoplasmic reticulum Ca^{2+} release produces Ca^{2+} microdomains in the T-SR model. (A-C) Heat map with overlaid 12 nm finite element mesh demonstrating steady state radial $[Ca^{2+}]$ gradients following application of Ca^{2+} influx density, J_{influx}, expected from a depolarizing step from the resting to a 0 mV test voltage in voltage clamped amphibian muscle fibre as described in previous reports[45]. Highest $[Ca^{2+}]$ is at the T-SR centres with ~ fivefold concentration reductions between the centre and edge in both (**A**), (**C**) T-tubular membrane and (**B**) SR membrane face. Edge concentrations are close between the two membranes. (**D–F**) The Ca^{2+} microdomains extend the entire axial T-SR distance. This is demonstrated in heat maps of: (**D**) radial $[Ca^{2+}]$ (vertical, z-axis) over the T-tubular membrane surface (xy-plane), more closely quantified by (**E**) midline axial section map of $[Ca^{2+}]$ taken along the y-axis. $[Ca^{2+}]$ plotted against radial distance along the T-tubular membrane in both x and y axes in (**D**) and in the y axis in (**E**). The jagged base of the surface plot is the result of interpolation of results from a cylindrical geometry. (**F**) $[Ca^{2+}]$ heatmap through midline axial section through the T-SR junction. Vertical axis plots axial (z) distance from the T-tubular membrane within the T-SR junction. Horizontal (x) axis plots radial distance from the T-SR junction centre. Colours represent the resulting steady state $[Ca^{2+}]$. Note uniformity in concentration along the z axis and fivefold gradients along the x axis. Colour bars in (**D**) and (**E**), and (**F**), show $[Ca^{2+}]$ as represented in the heat maps. (**G–I**) Time course of microdomain $[Ca^{2+}]$ solutions at selected positions within the T-SR junction. (**G**) Solutions for $[Ca^{2+}]$ at the edge (black), centre (blue) of the T-SR junction and midway between these two (red lines) plotted against time following initiation of the Ca^{2+} influx, J_{influx} from the SR face of the T-SR junction. Initial instabilities in plots observed in the edge traces reflect stiff-stable properties of the solutions. (**H**) Variations in steady state $[Ca^{2+}]$ with radial distance from the centre of the T-SR junction parallel to the radial axis at the T-tubular membrane, the SR membrane, or halfway between these. (**I**) $[Ca^{2+}]$ plotted with time following the onset of Ca^{2+} influx, but with its termination after 0.5 ms.

was assigned a number referenced using a command retrieving the solution from the node closest to a specified 3-dimensional Cartesian co-ordinate (https://www.mathworks.com/help/pde/ug/heat-transfer-problem-with-temperature-dependent-properties.html). The solution from the node closest to selected points representing the edge and centre of the geometry, and half-way between these was plotted against time through the time trajectory of the computation (Fig. 2G). These typically reached steady state over a ~ 0.2 ms exponential timecourse following the onset of the imposed J_{influx}, a timescale ~ 1–2 orders of magnitude shorter than experimentally measured Ca^{2+} transients in vivo[45]. The resulting steady state $[Ca^{2+}]$ at axial distances within the T-SR junction could additionally be obtained by interpolation for plotting against radial distance from the centre of the T-SR junction (Fig. 2H). Comparing $[Ca^{2+}]$ timecourses with imposition and termination of the Ca^{2+} fluxes confirmed that $[Ca^{2+}]$ recovered back to its initial starting value, as expected for a first-order diffusional system (Fig. 2I). Finally, solutions obtained using varying 6 nm and 3 nm mesh sizes gave $[Ca^{2+}]$ microdomain characteristics in close agreement, validating the computational parameters used in our finite element analysis (Supplementary Table S1).

Persistent Ca^{2+} microdomains with $[Ca^{2+}]$ graded with Ca^{2+} flux densities through varied test voltages. The T-SR junction model was then tested against varying J_{influx} holding constant the remaining diffusional, D and λ, and T-SR geometrical parameters, d and w (Supplementary Table S2). The J_{influx} values used were calculated from previous experimental $d[Ca^{2+}]/dt$ produced by varying steps to physiologically activating depolarizing test voltages (Table 1). Microdomain T-SR centre and $[Ca^{2+}]_{edge}$ changes were then compared with corresponding experimental peak changes in intracellular Ca^{2+} concentrations $[Ca^{2+}]_{max}$, at the same test voltage[45].

Firstly, all the test voltages were associated with T-SR junction Ca^{2+} microdomains (Fig. 3). Figure 3A plots diffusion equation solutions with time after imposing the Ca^{2+} influx to reach steady state $[Ca^{2+}]$ values at the centre and edge of the T-SR junction, and halfway between these points. Figure 3B shows these dependences of the steady state $[Ca^{2+}]$ with radial distance close to the T-tubular (superscript 'T') and SR membranes (superscript 'SR'), and halfway along their axial distance (superscript 'TSR'). $[Ca^{2+}]$ declined from its maximum values with radial distance from the T-SR junction centre (subscripts below: 'centre') towards the T-SR edge (subscript 'edge') with similar readouts close to the T-tubular (subscript: 'T') and SR membranes (subscript: 'SR'), and half-way (subscript: '50%') along their axial distance.

Secondly, quantifications of Ca^{2+} microdomains arising from the range of J_{influx} values and corresponding test voltages showed that these were similar in form, consistent with the linearity expected of diffusional processes. This emerged from comparing ratios between $[Ca^{2+}]$ at the T-SR centre with those at the edge and halfway between (50%) at the T-tubular and SR membranes, and within the T-SR space. Thus $[Ca^{2+}]^T_{50\%}/[Ca^{2+}]^T_{centre}$, $[Ca^{2+}]^{TSR}_{50\%}/[Ca^{2+}]^{TSR}_{centre}$, and $[Ca^{2+}]^{SR}_{50\%}/[Ca^{2+}]^{SR}_{centre}$ values were all close to 79% and $[Ca^{2+}]^T_{edge}/[Ca^{2+}]^T_{centre}$, $[Ca^{2+}]^{TSR}_{edge}[Ca^{2+}]^{TSR}_{centre}$ and $[Ca^{2+}]^{SR}_{edge}/[Ca^{2+}]^{SR}_{centre}$ were all close to 14%. Similarly, the radial distances from the T-SR centre over which $[Ca^{2+}]$ fell by 50% of its centre-edge range were all 77.67, 77.90 and 77.76 nm whether close to the T-tubular membrane, the SR membrane and halfway between these respectively.

Thirdly, progressively larger J_{influx} values corresponding to the increasing experimental $d[Ca^{2+}]/dt$ with progressive depolarization correspondingly predicted increased steady state $[Ca^{2+}]$ whether at the centre, 50% from or at the T-SR edge, or close to T-tubular or SR membranes or between these. They produced substantially higher, ~ 10's of μM $[Ca^{2+}]$ values at the T-SR centre than the ~ μM $[Ca^{2+}]$ values at the edge.

Both the individual values of, and the relationships between, the modelled J_{influx} at differing test voltages and $[Ca^{2+}]_{edge}$ closely matched the corresponding reported experimental relationship between $d[Ca^{2+}]/dt$ and $[Ca^{2+}]_{max}$. Figure 3C shows that the voltage-matched J_{influx} values gave $[Ca^{2+}]_{edge}$ values similar to those of the corresponding reported experimental $[Ca^{2+}]_{max}$[45]. Figure 3D shows a linear relationship between $[Ca^{2+}]_{edge}$, and
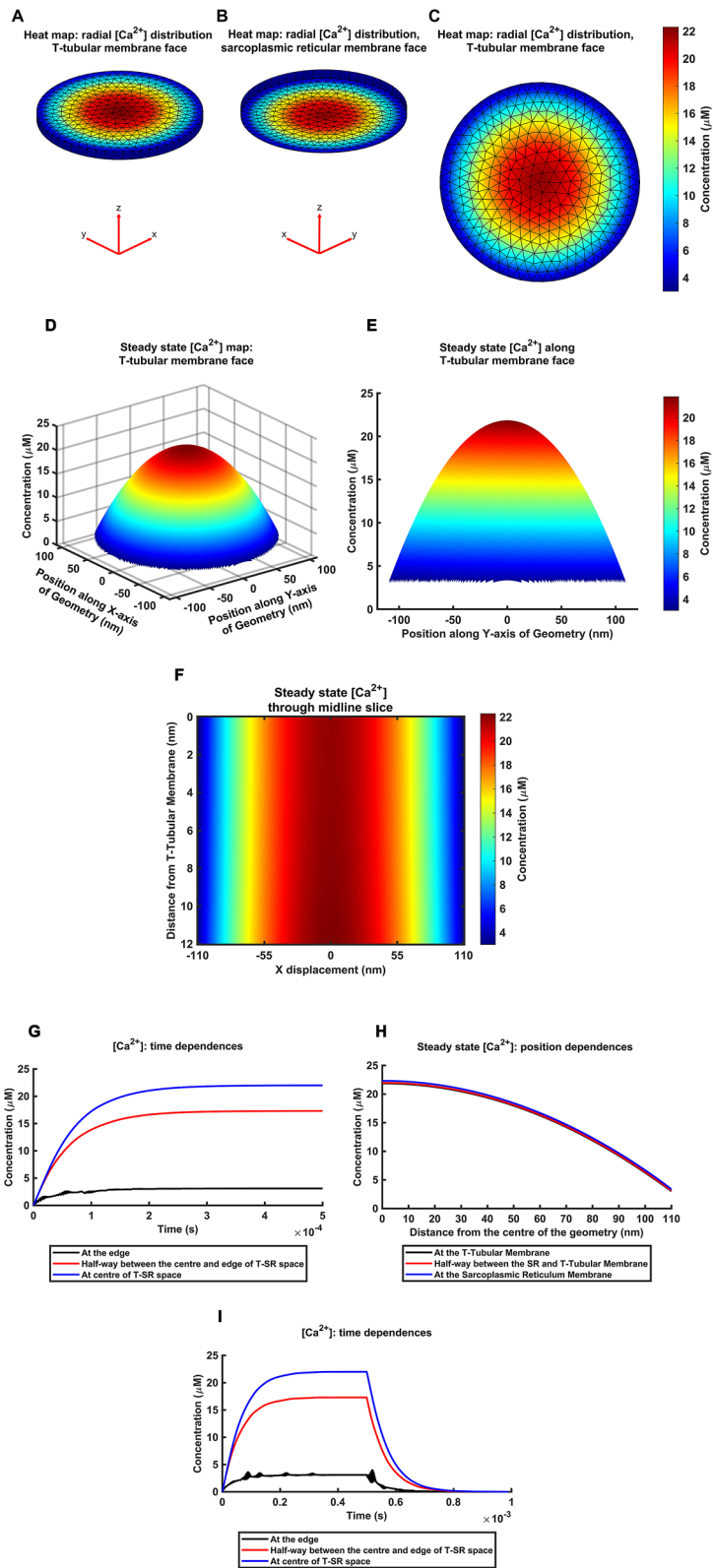
Figure 3. Ca²⁺ microdomains reconstructed using varied Ca²⁺ flux densities derived from experimental Ca²⁺ transients in response to test voltage steps. (**A**, **B**) Persistent Ca²⁺ microdomains with [Ca²⁺] magnitudes graded with experimentally derived Ca²⁺ influx densities J_{influx} corresponding to varying experimental test voltage steps applied to amphibian muscle fibres[45]. (**A**) [Ca²⁺] changes with time following onset of the imposed J_{influx} and (**B**) the resulting dependences of the steady state changes in [Ca²⁺] upon radial distances from the centre of the T-SR junction. The [Ca²⁺] across the T-SR junction falls with reducing depolarizing steps at all points in both the steady state and with time. For comparison, the y axis limit has been fixed at 25 μM. (**C–E**) The T-SR model recapitulates experimentally reported Ca²⁺ flux densities and resulting Ca²⁺ concentrations following the graded test voltage steps. Thus: (**C**) Measured cytoplasmic [Ca²⁺] (filled symbols) achieved following test voltage steps [45] compared with [Ca²⁺]$_{edge}$ (open symbols) in response to Ca²⁺ flux densities, J_{influx} determined from reported rates of increase in [Ca²⁺], d[Ca²⁺]/dt, corresponding to those test voltages (abscissa) illustrated in (**A**, **B**) at exit length $λ = 9.2$ nm. (**D**) Plot of [Ca²⁺]$_{edge}$ from the reconstructed T-SR junction against reported cytoplasmic [Ca²⁺][45]. The points fit a linear regression model with a gradient close to 1 (1.02) and intercepts close to the origin. (**E**) Plot of Ca²⁺ influx across the SR membrane $Φ_{influx}$ against computed [Ca²⁺]$_{edge}$ expressed in SI units. The points fit a linear regression model with a gradient and zero intercept matching that expected from the conservation condition. The matching computed and observed [Ca²⁺] in (**C**) and the gradients and intercepts in (**D**) and (**E**) confirm match of the T-SR junction model to previous experimental results at different test voltages.

[Ca²⁺]$_{max}$ with close to unity gradient and zero intercept. Furthermore, combining the Ca²⁺ influx and efflux equality condition, $Φ_{influx} = Φ_{efflux}$, and the efflux equation (Eqs. 7–9) gives the conservation relationship:

$$\Phi_{efflux} = J_{efflux}\pi\,dw = \frac{D\left[Ca^{2+}\right]_{edge}}{\lambda}(\pi\,dw) \tag{15}$$

This yielded data points replicating the predicted linear dependence between $Φ_{influx}$ and [Ca²⁺]$_{edge}$. This had a zero intercept and slope in agreement with the efflux prediction $\frac{\Phi_{efflux}}{[Ca^{2+}]_{edge}} = \frac{D}{\lambda}(\pi\,dw) = 3.606 \times 10^{-17}$ m³/s (Fig. 3E). Finally, in accord with linearity predictions, computations adopting further tenfold J_{influx} reductions similarly (A) converged monotonically to steady state [Ca²⁺] measurable at selected radial distances from the T-SR junction centre yielding (B) uniform radial [Ca²⁺] gradients along the T-SR distance visualized as (C) radial [Ca²⁺] gradients extending the full axial T-SR junction distance (Supplementary Table S3 and Fig. S2). The [Ca²⁺]$^T_{50\%}$/[Ca²⁺]$^T_{centre}$, [Ca²⁺]$^{TSR}_{50\%}$/[Ca²⁺]$^{TSR}_{centre}$, and [Ca²⁺]$^{SR}_{50\%}$/[Ca²⁺]$^{SR}_{centre}$ as well as the [Ca²⁺]$^T_{edge}$/[Ca²⁺]$^T_{centre}$, [Ca²⁺]$^{TSR}_{edge}$/[Ca²⁺]$^{TSR}_{centre}$ and [Ca²⁺]$^{SR}_{edge}$/[Ca²⁺]$^{SR}_{centre}$ remained essentially constant (79% and 14%). Furthermore, radial distances from the T-SR centre over which [Ca²⁺] fell by 50% of its centre-edge range, whether close to the T-tubular membrane, the SR membrane and half way between these respectively remained similar (77.67, 77.90 and 77.76 nm). [Ca²⁺] levels through the T-SR junction fell proportionally with 10- and 100-fold J_{influx} reductions: [Ca²⁺]$^T_{centre}$ fell from ~ 0.43 μM to 0.043 μM and 0.0043 μM respectively, as expected from the relationship established in Fig. 3E.

Ca²⁺ microdomains with varied Ca²⁺ diffusion coefficients.

Skeletal muscle T-SR junction properties vary with physiological conditions, both within and between muscle fibres, individual muscles and muscle types. Furthermore, such surface-cytoplasmic membrane appositions also occur in and vary amongst other cell types. Nevertheless, the Ca²⁺ microdomains robustly persisted with wide variations involving previously experimentally reported Ca²⁺ diffusion constants, D, and T-SR junction geometries represented by their axial distances w, and diameters, d. These further computations varied each parameter in turn holding the remaining variables constant under conditions of fixed J_{influx}.

Firstly, we extended the modelling beyond the reported skeletal muscle cytosolic Ca²⁺ diffusion coefficient $D = 4.0 \times 10^7$ nm²/s[46–48]. Higher reported values reach 5.2×10^8 nm²/s in other cell types[50] (cf:[51–54]) and 1×10^9 nm²s at infinite dilution in vitro[55,56] (Supplementary Table S4). Lower D values might result from local concentrations of proteins, lipids or ions, suggested by the reported electron-dense T-SR junction cytosol[44]. Solutions with D between 4.0×10^5 and 1×10^9 nm²/s at constant w, d and J_{influx}, continued to converge with correspondingly varied relative timescales (Fig. 4A). They predicted steady state radial [Ca²⁺] gradients extending the full axial distance between T and SR membranes (Fig. 4B,C). Radial dependences of [Ca²⁺] with distance from the T-SR centre (Fig. 4B) were not altered by the changes in D. Ratios between [Ca²⁺] at the edge and halfway from the centre, to [Ca²⁺] at the T-SR centre whether close to T-tubular or SR or between the two membranes, remained at 79% and 14% respectively. Distances for [Ca²⁺] to fall to 50% between centre and edge values similarly remained unchanged. However, diffusion coefficient value markedly influenced [Ca²⁺] at the centre of the T-SR junction.

Nevertheless, even the highest $D = 1 \times 10^9$ nm²/s free diffusion value at infinite dilution predicted near μM-[Ca²⁺] microdomains. Conversely, successive tenfold reductions in D down to 4.0×10^5 nm²/s resulted in limiting ~ mM hypothetical TSR [Ca²⁺] levels approaching reported in situ free SR [Ca²⁺] (~ 3.6 mM; assuming a 6.1 mM SR [calsequestrin] with a 1.1 mM Ca²⁺ binding constant[57]). Plotting $\log_{10}$[Ca²⁺] values at the centre, edge of the T-SR junction, and halfway between these against $\log_{10}(D)$ all yielded similar linear plots reflecting the constant radial [Ca²⁺] profiles shown by the Ca²⁺ microdomains (Fig. 4D). Their constant gradient indicated inverse [Ca²⁺]-D relationships and a $\{[Ca^{2+}]_{edge}/(1/D)\}$ proportionality constant, 1.27×10^{-13} mol/(ms) agreeing with the steady state $Φ_{influx} = Φ_{efflux}$ conservation condition for which:
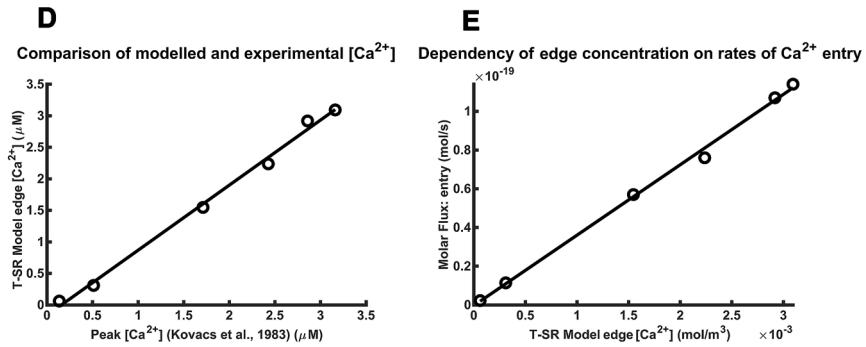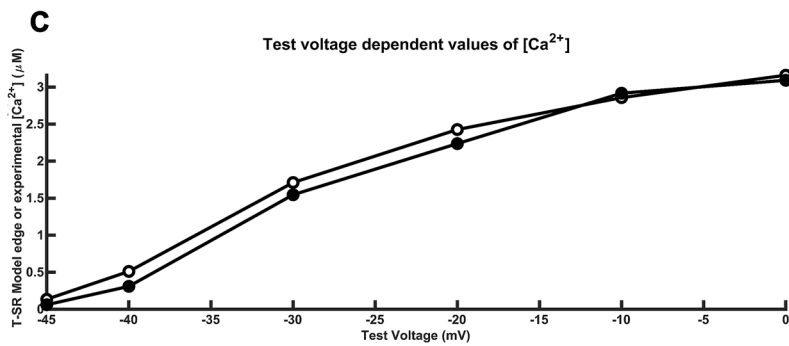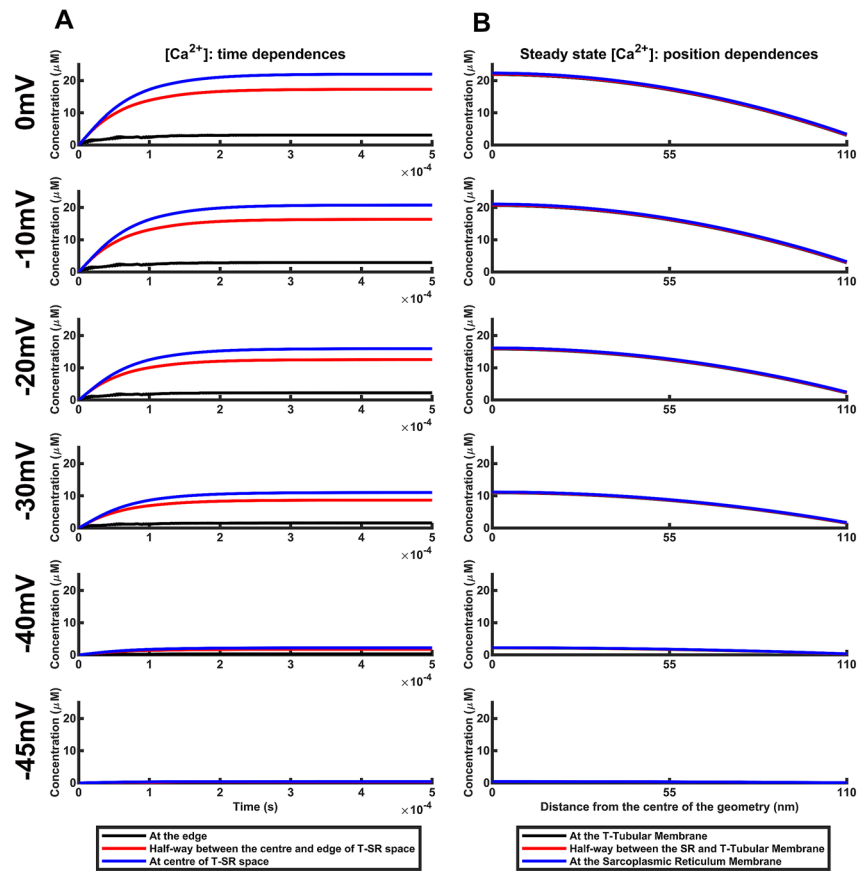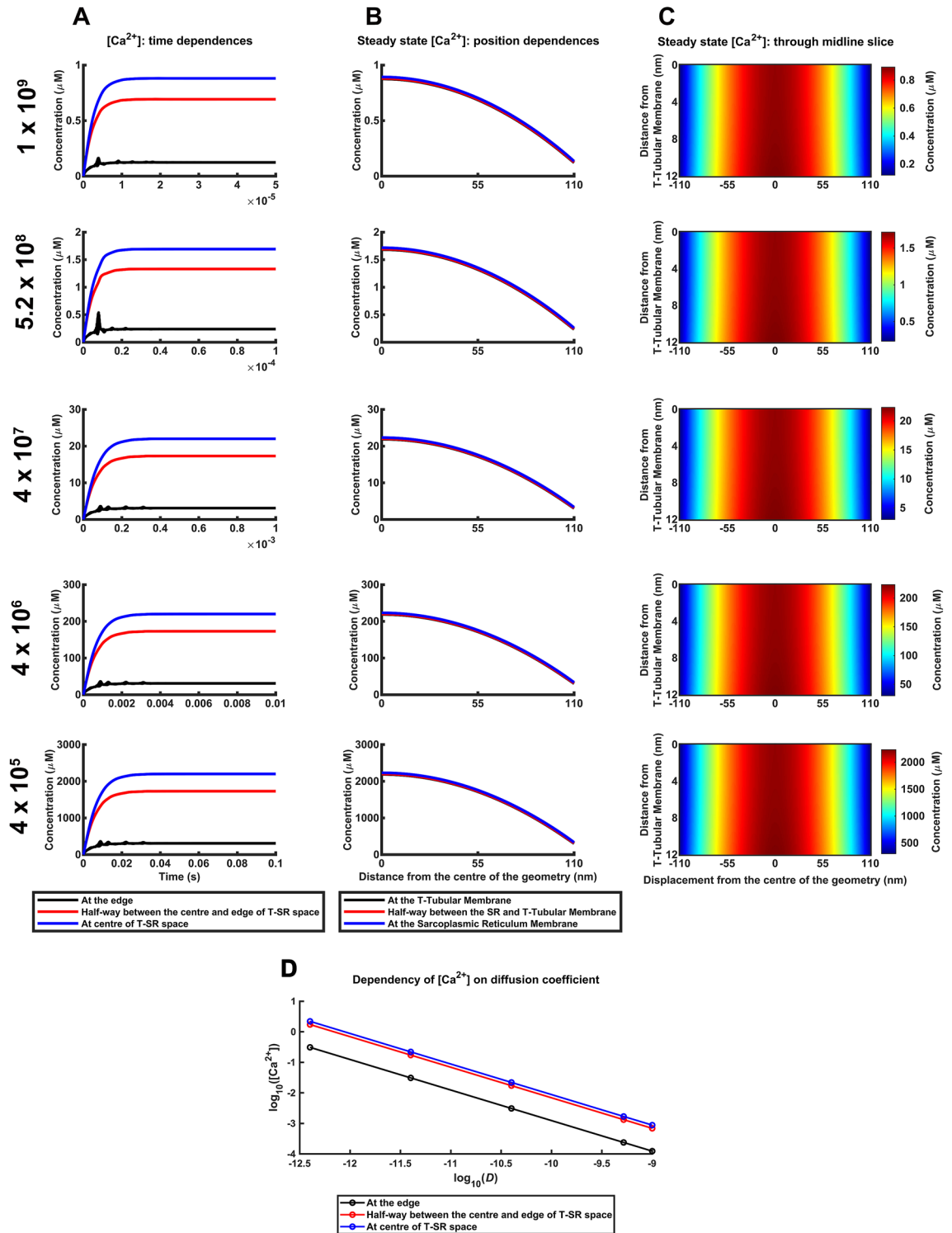
Figure 4. Ca²⁺ microdomain characteristics persist with variation in Ca²⁺ diffusion coefficient. (A-C) Exploring effects of variations in reported in vitro and in vivo Ca²⁺ diffusion coefficient values (units: nm²/s), D, ranging from highest reported values at infinite dilution, through two reported in vivo values, and two substantially lower values for comparison. Ca²⁺ influx density, J_{influx}, T-SR diameter, d, and T-SR distance, w, maintained constant at values adopted in the T-SR model (Table 1). (**A**) Variations in [Ca²⁺] with time following onset of imposed J_{influx}. (**B**) Dependence of the resulting steady state [Ca²⁺] with radial distance from the centre of the T-SR junction. (**C**) Mapping of [Ca²⁺] across a midline axial slice; values of [Ca²⁺] scaled linearly with maximum [Ca²⁺] at centre of T-SR junction to illustrate features of microdomain characteristics and radial concentration gradients. (**D**) Inverse relationship between [Ca²⁺] at the centre, the edge, and halfway between these of the T-SR junction, and diffusion coefficient, D. Linear double logarithmic plots of $[Ca^{2+}]^{TSR}_{centre}$, $[Ca^{2+}]^{TSR}_{50\%}$ and $[Ca^{2+}]^{TSR}_{edge}$, against diffusion coefficient, D, coefficients corresponding to an inverse relationship between $[Ca^{2+}]^{TSR}_{centre}$, $[Ca^{2+}]^{TSR}_{50\%}$ and $[Ca^{2+}]^{TSR}_{edge}$, and D, at constant Ca²⁺ influx density, J_{influx}, T-SR diameter, d, and T-SR distance, w.

$$[\text{Ca}^{2+}]_{\text{edge}} = \left(\frac{\lambda d J_{\text{influx}}}{4wD} \right) \qquad (16)$$

Ca²⁺ microdomains at increased T-SR distances. Secondly, T-SR distances also vary with physiological conditions (Supplementary Table S5). They fall from $w = 12$ nm to 6.6 nm in hypertonic extracellular solutions[58]. They increase to 20.15 nm and 29.60 nm with fatiguing low-frequency intermittent stimulation[59] and exposure to hypotonic solutions[60] respectively. Computational solutions modelling these variations in w at constant J_{influx}, D and d (Fig. 5) showed early instabilities with time at the greatest w values (Fig. 5A). Nevertheless, all solutions ultimately converged to steady state Ca²⁺ microdomains with increased [Ca²⁺] at the T-SR centre declining with radial distance. However, differences between [Ca²⁺] values close to the SR, the T-tubular membranes, and within the intervening space occurred at the greater T-SR distances (Fig. 5B). The colourmaps then correspondingly showed marked axial, in addition to radial [Ca²⁺] non-uniformities (Fig. 5C) with a plume-like tapering. This contrasts with the small axial nonuniformities at $w = 12$ nm becoming even smaller with its reduction to $w = 6.6$ nm. This also directly contrasts with the previous near-uniform Ca²⁺ microdomain radial profiles through the entire T-SR junctional distance observed in the computations varying J_{influx} and D.

Quantification of these effects as w increased from 6 to 30 nm, showed that close to the T-tubular membrane, $[\text{Ca}^{2+}]^{\text{T}}_{50\%}/[\text{Ca}^{2+}]^{\text{T}}_{\text{centre}}$ and $[\text{Ca}^{2+}]^{\text{T}}_{\text{edge}}/[\text{Ca}^{2+}]^{\text{T}}_{\text{centre}}$ remained at ~79% and ~14% respectively. Similarly at the midpoint between T-tubular and SR membranes, $[\text{Ca}^{2+}]^{\text{TSR}}_{50\%}/[\text{Ca}^{2+}]^{\text{TSR}}_{\text{centre}}$ and $[\text{Ca}^{2+}]^{\text{TSR}}_{\text{edge}}/[\text{Ca}^{2+}]^{\text{TSR}}_{\text{centre}}$ were ~78% and ~13% respectively. However, close to SR membrane, $[\text{Ca}^{2+}]^{\text{SR}}_{50\%}/[\text{Ca}^{2+}]^{\text{SR}}_{\text{centre}}$ and $[\text{Ca}^{2+}]^{\text{SR}}_{\text{edge}}/[\text{Ca}^{2+}]^{\text{SR}}_{\text{centre}}$ increased to ~80% and ~18% respectively. Furthermore, the axial nonuniformities in [Ca²⁺] close to the SR and T-tubular membranes involved both the centre and edge of the T-SR junction. Thus, $[\text{Ca}^{2+}]^{\text{SR}}_{\text{centre}}/[\text{Ca}^{2+}]^{\text{T}}_{\text{centre}}$ increased from 1.005 to 1.133 and $[\text{Ca}^{2+}]^{\text{SR}}_{\text{edge}}/[\text{Ca}^{2+}]^{\text{T}}_{\text{edge}}$ increased from 1.031 to 1.565.

In addition, radial distances for [Ca²⁺] to fall to 50% as a fraction of the total T-SR radius showed contrasting patterns at the T-tubular and SR membranes with increasing w. $X_{\text{centre}}/$(T-SR radius) then fell from 0.763 to 0.748 whereas $X_{\text{edge}}/$(T-SR radius) increased from 0.765 to 0.793. Finally, both steady state centre and edge [Ca²⁺], whether at the T-tubular or SR membranes, or within the T-SR junction, decreased. Thus, $[\text{Ca}^{2+}]^{\text{T}}_{\text{centre}}$ and $[\text{Ca}^{2+}]^{\text{T}}_{\text{edge}}$ fell from 43.965 and 6.190 to 8.428 and 1.081 respectively. Nevertheless, even the lowest values of $[\text{Ca}^{2+}]^{\text{T}}_{\text{edge}}$ resulted in µM-[Ca²⁺] changes. Finally, $[\text{Ca}^{2+}]_{\text{edge}}$ inversely depended upon w (Fig. 5D). The $\left([\text{Ca}^{2+}]_{\text{edge}} w \right)$ proportionality constant (3.57×10^{-11} mol/m²) approximated predictions from parameter values in the steady state conservation condition $[\text{Ca}^{2+}]_{\text{edge}} = \left(\frac{d\lambda J_{\text{influx}}}{4Dw} \right)$, giving $\left(\frac{d\lambda J_{\text{influx}}}{4D} \right) = 3.79 \times 10^{-11}$ mol/m².

Ca²⁺ microdomains at decreased T-SR diameters. Thirdly, significant variations in effective areas of membrane appositions occur not only between skeletal muscle T-tubular and SR membrane but also occur in and between other cell types. We quantified these effects successively reducing T-SR junction diameters, d, from the initial 220 nm down to 40 nm, at constant J_{influx}, D and w (Fig. 6, Supplementary Table S6). The computational solutions showed some initial instabilities but ultimately converged even at the smallest T-SR diameters (Fig. 6A). They similarly generated Ca²⁺ microdomains in which [Ca²⁺] declined with radial distance from the T-SR junction centre. These radial gradients accompanied significant axial [Ca²⁺] variations at the T-tubular and SR membranes and the intervening space (Fig. 6B) resulting in plume-like tapering at the smallest T-SR diameters in the colourmaps (Fig. 6C).

Quantifications of these alterations in Ca²⁺ microdomain characteristics first demonstrated changes in $[\text{Ca}^{2+}]^{\text{T}}_{50\%}/[\text{Ca}^{2+}]^{\text{T}}_{\text{centre}}$ and $[\text{Ca}^{2+}]^{\text{T}}_{\text{edge}}/[\text{Ca}^{2+}]^{\text{T}}_{\text{centre}}$ from 78 and 14% respectively at $d = 220$ nm to 86% and 45% at $d = 40$ nm. There were also significant [Ca²⁺] differences between T-SR regions close to the T-tubular and SR membranes with $[\text{Ca}^{2+}]^{\text{SR}}_{\text{centre}}/[\text{Ca}^{2+}]^{\text{T}}_{\text{centre}}$ and $[\text{Ca}^{2+}]^{\text{SR}}_{\text{edge}}/[\text{Ca}^{2+}]^{\text{T}}_{\text{edge}}$ at 1.021 and 1.111 at $d = 220$ nm to 1.426 and 1.689 at $d = 40$ nm. The distances through which [Ca²⁺] fell to half of its maximum value as a proportion of T-SR radius ($X_{\text{centre}}/$(T-SR radius)) and ($X_{\text{edge}}/$(T-SR radius)) increased from 0.761 to 0.768 and 0.950 to 1.000 respectively. Finally, $[\text{Ca}^{2+}]^{\text{T}}_{\text{centre}}$ and $[\text{Ca}^{2+}]^{\text{T}}_{\text{edge}}$ fell from 21.876 and 3.025 to 1.047 and 0.473 respectively. Thus, even a $d = 40$ nm diameter produced µM-[Ca²⁺] microdomain differences. $[\text{Ca}^{2+}]_{\text{edge}}$ positively correlated with d, with slopes between 1.41×10^4 to 1.35×10^4 mol/m⁴ in agreement with steady state flux conservation, giving $[\text{Ca}^{2+}]_{\text{edge}} = \frac{\lambda d J_{\text{influx}}}{4Dw}$ for which $\frac{\lambda J_{\text{influx}}}{4Dw} = 1.44 \times 10^4$ mol/m⁴ (Fig. 6D).

Ca²⁺ microdomains in resting muscle fibres. Finally, the recent reports that had suggested an existence of T-SR junction Ca²⁺ microdomains included evidence suggesting background ryanodine receptor (RyR)-mediated Ca²⁺ fluxes modulating Na$_{\text{v}}$1.4 function even in resting skeletal muscle[27,30]. Available Fura-2 studies suggest resting cytosolic [Ca²⁺] between 0.06 and 0.14 µM[61]. The highest reported, Fluo-3, studies reported up to 0.30 µM[62,63] and the lowest Ca²⁺-sensitive microelectrode measurements, 0.038 µM[64] (Supplementary Table S7). These reports permitted determination of values for the corresponding background J_{influx} from the influx and efflux equations for Φ_{influx} and Φ_{efflux} respectively, assuming the conservation condition $\Phi_{\text{influx}} = \Phi_{\text{efflux}}$. Approximating these [Ca²⁺] values to $[\text{Ca}^{2+}]_{\text{edge}}$ would give the required $J_{\text{influx}} = \frac{4Dw[\text{Ca}^{2+}]_{\text{edge}}}{\lambda d}$. Employing this resting myoplasmic [Ca²⁺] range (Fig. 7A) indicated the existence of Ca²⁺ microdomains with radial concentration profiles (Fig. 7B,C), ratios of [Ca²⁺] at the edge and halfway between edge and centre, and the centre (79% and 14%), and X'_{centre}, $X'_{50\%}$, and X'_{rim} values (77.67, 77.76 and 77.90 nm) all identical to corresponding values at higher J_{influx}. Finally, the $[\text{Ca}^{2+}]^{\text{T}}_{\text{centre}}$, $[\text{Ca}^{2+}]^{\text{TSR}}_{\text{centre}}$ and $[\text{Ca}^{2+}]^{\text{SR}}_{\text{centre}}$ approached 1 µM [Ca²⁺] concentrations, giving 0.268, 0.270 and 0.274 at the lowest and 0.990, 0.995 and 1.010 µM at the highest resting [Ca²⁺].
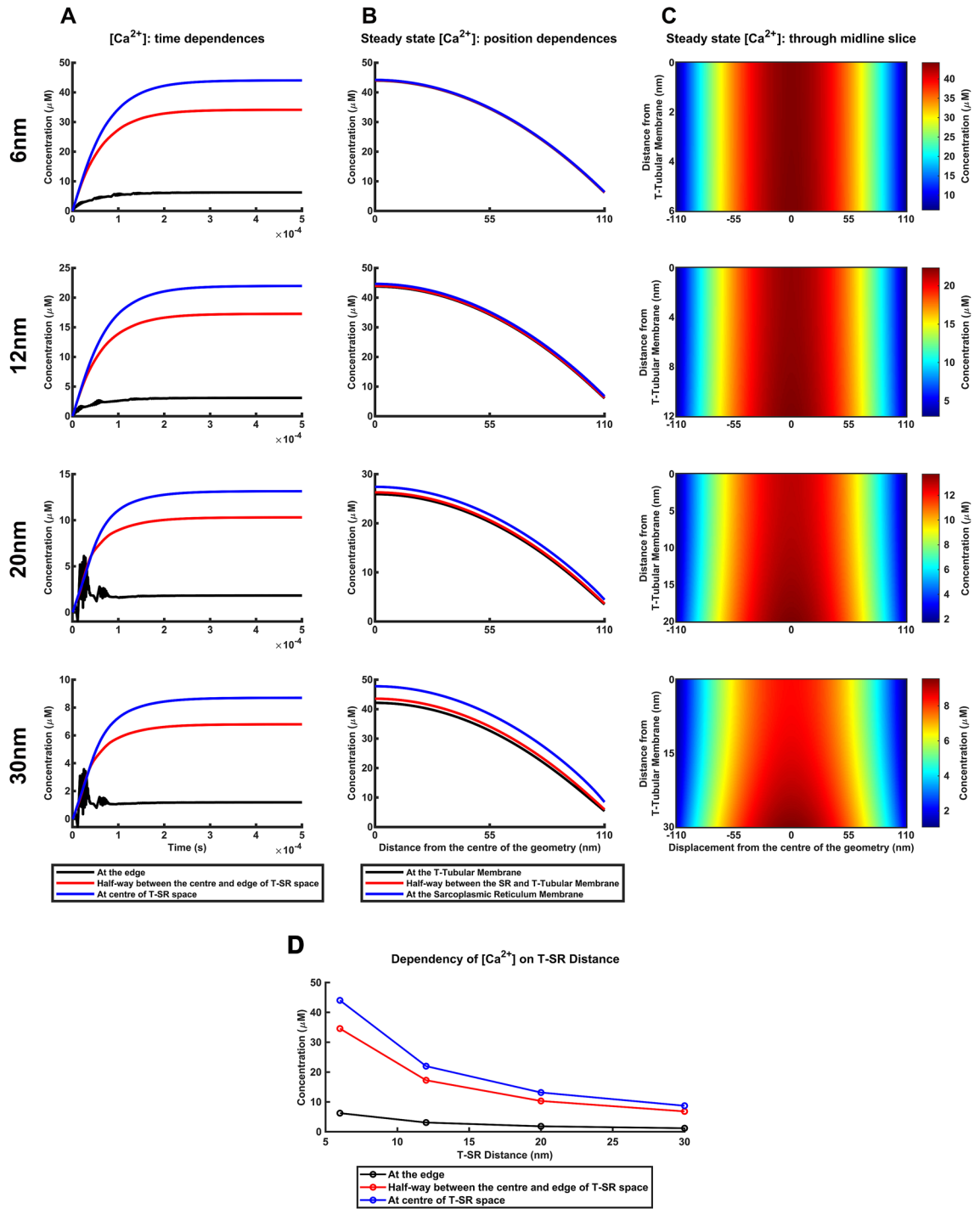
Figure 5. Altered Ca^{2+} microdomain characteristics with increased T-SR distances.. (**A**-**C**) The effect of variations in reported experimental values of T-SR distance, w, ranging from lowest reported values in hypertonic extracellular conditions to the greatest values associated with fatiguing exercise at constant imposed Ca^{2+} influx density, J_{influx} diffusion coefficient, D, and TSR diameter, d. (**A**) Variations in [Ca^{2+}] with time following onset of imposed J_{influx}. (**B**) Resulting variations in steady state [Ca^{2+}] with radial distance from the centre of the T-SR junction; note significant differences in the [Ca^{2+}] magnitudes close to the T-tubular, the sarcoplasmic reticular (SR) membranes, and the intervening T-SR region. (**C**) Mapping of [Ca^{2+}] across a midline axial slice; values of [Ca^{2+}] are scaled linearly with maximum concentration at centre of T-SR junction [Ca^{2+}] to illustrate features of microdomain characteristics and the radial concentration gradients. Note marked pluming of the Ca^{2+} microdomain with increasing T-SR distance. (**D**) Dependence of T-SR junctional [Ca^{2+}] at the centre, the edge, and halfway between these upon T-SR distance, w. Relationships emerging from plots of [Ca^{2+}]$^{TSR}_{centre}$, [Ca^{2+}]$^{TSR}_{50\%}$ and [Ca^{2+}]$^{TSR}_{edge}$, against T-SR distance, w, at constant diffusion coefficient, D, influx density, J_{influx} and T-SR diameter, d.
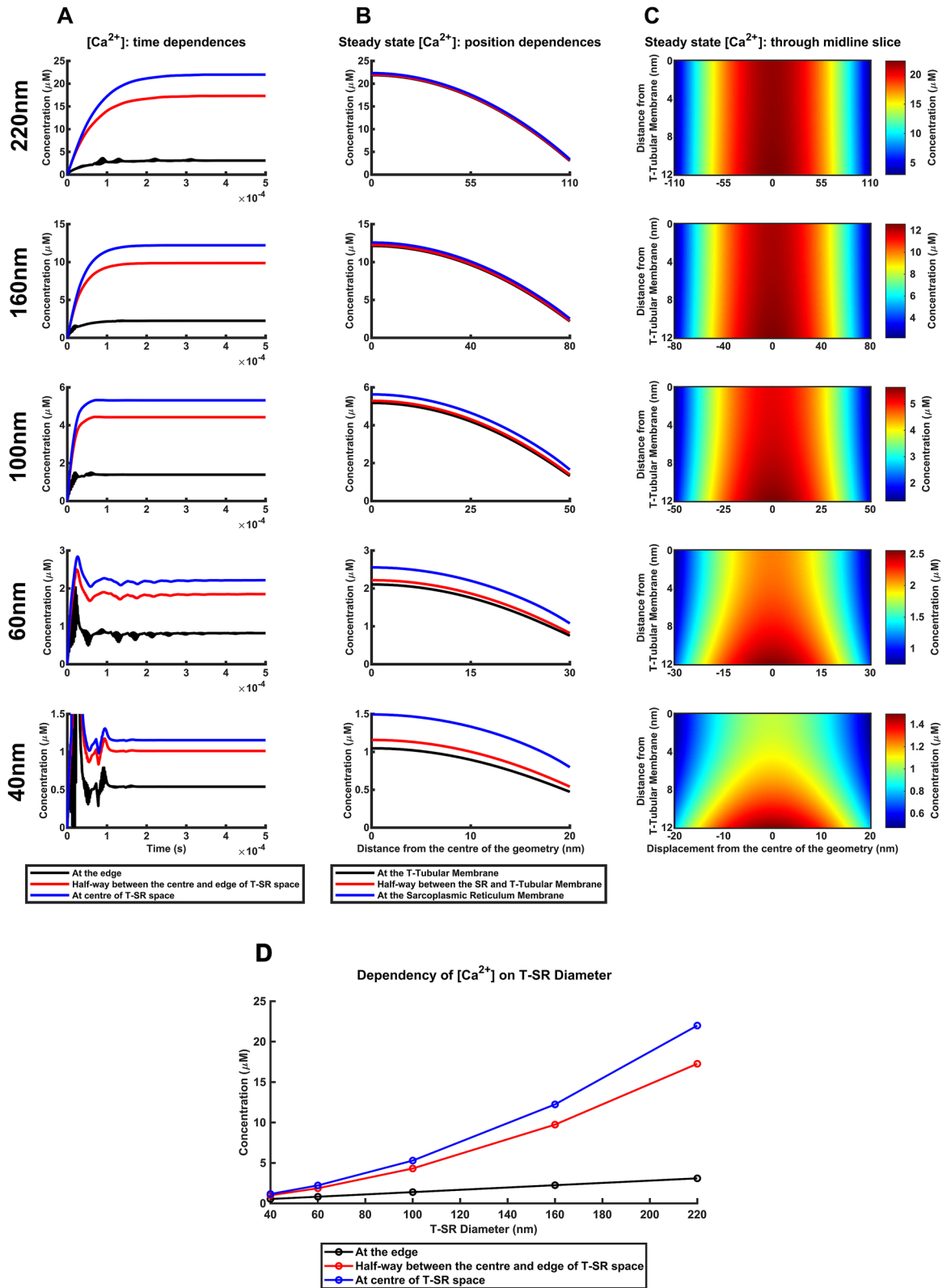
Figure 6. Calcium microdomain stability breaks down at decreased T-SR diameters. (**A–C**) Effect of reductions in T-SR diameter, *d*, from value adopted in the T-SR model. Computations at constant imposed Ca²⁺ influx density, J_{influx}, diffusion coefficient, *D*, and T-SR distance, *w*. (**A**) Variations in [Ca²⁺] with time following onset of imposed J_{influx}. Note initial instabilities close to the onset of imposition of J_{influx} at the reduced T-SR diameters. (**B**) Resulting variations in steady state [Ca²⁺] with radial distance from the centre of the T-SR junction; note significant differences in the regions close to the T-tubular and sarcoplasmic reticular (SR) membranes, and the intervening T-SR region with decreasing T-SR diameter, *d* (**C**) Mapping of [Ca²⁺] across a midline axial slice; values of [Ca²⁺] are scaled linearly with maximum concentration at centre of T-SR junction [Ca²⁺] to illustrate microdomain characteristics and radial concentration gradients. Marked pluming of Ca²⁺ microdomain with decreasing T-SR diameter. (**D**) Dependence of T-SR junctional [Ca²⁺] at the centre, the edge, and halfway between these upon T-SR diameter. Relationships emerging from plots of $[Ca^{2+}]^{TSR}_{centre}$, $[Ca^{2+}]^{TSR}_{50\%}$ and $[Ca^{2+}]^{TSR}_{edge}$, against TSR diameter, *d*, at constant diffusion coefficient, *D*, influx density, J_{influx} and T-SR distance *w*.
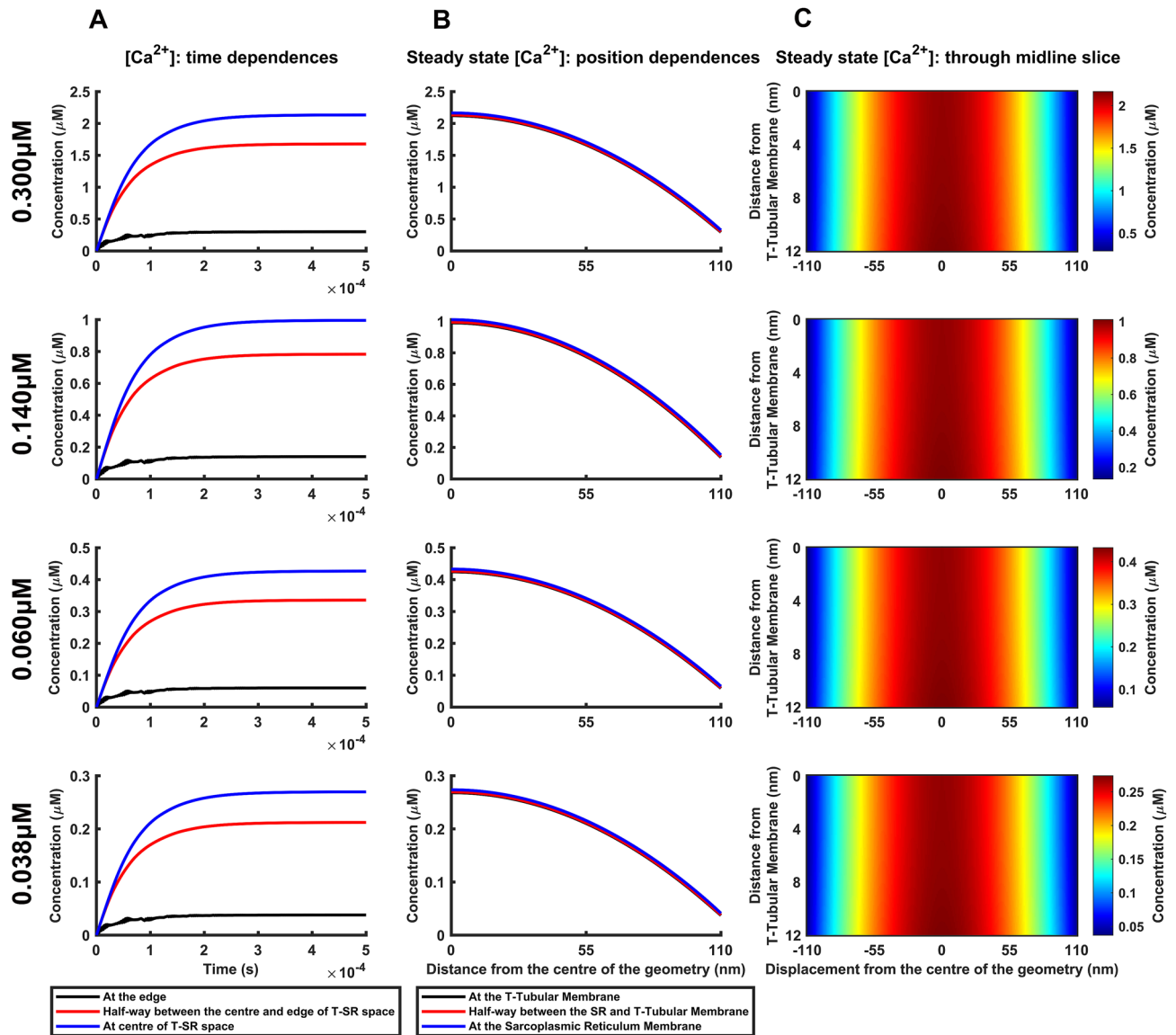
Figure 7. Ca^{2+} microdomains attain micromolar $[Ca^{2+}]$ levels at edge $[Ca^{2+}]$ corresponding to resting $[Ca^{2+}]$. Effects of variations in Ca^{2+} influx density, J_{influx}, generating T-SR junction edge Ca^{2+} concentrations, $[Ca^{2+}]_{edge}$ achieving previously reported resting $[Ca^{2+}]$ levels studied at constant values of diffusion coefficient, D, T-SR diameter, d, and distance, w. (**A**) Variations in $[Ca^{2+}]$ with time following onset of imposed J_{influx}. (**B**) Resulting variations in steady state $[Ca^{2+}]$ with radial distance from the centre of the T-SR junction. (**C**) Mapping of $[Ca^{2+}]$ across a midline axial slice; values of $[Ca^{2+}]$ are scaled linearly with maximum concentration at centre of T-SR junction $[Ca^{2+}]$ to illustrate persistence and features of microdomains including their radial concentration gradients.

Physiological implications of modelled T-SR junction Ca^{2+} microdomains. Together, the present findings substantiate recent experimental reports predicting physiologically significant T-SR Ca^{2+} microdomains in skeletal muscle. These had implicated RyR-mediated SR Ca^{2+} release in modulating tubular $Na_v1.4$ function in both activated and resting skeletal muscle[27,30]. The spatial $[Ca^{2+}]$ data arrays obtained from the model of activated (Fig. 3; Table 1) and resting muscle (Fig. 7) were used to derive the respective proportions of T-tubular membrane facing the T-SR junction model exposed to different microdomain $[Ca^{2+}]$ (Fig. 8). In activated muscle, successively greater proportions of such T-tubular membrane became exposed to successively higher, 0.1 to 10 μM $[Ca^{2+}]$ with increasing depolarization (Fig. 8A). The latter included exposures to concentrations exceeding the 1.0 μM $[Ca^{2+}]$ levels corresponding to dissociation constants, K_d of typical modulatory proteins including calmodulin. Furthermore, the tested values of resting $[Ca^{2+}]$ similarly predicted exposures of significant proportions of T-tubular membrane to lower, but nevertheless significant, 0.5 μM $[Ca^{2+}]$ (Fig. 8B).
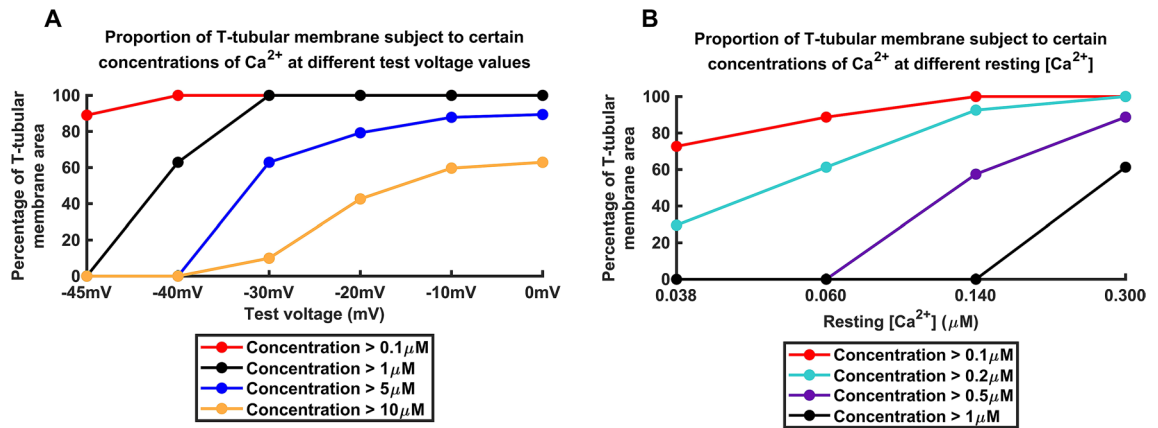
Figure 8. Proportions of T-SR junction T-tubular membrane area exposed to varied tested microdomain [Ca²⁺]. Results shown for (**A**) active muscle at different test voltages (Fig. 3) and (**B**) resting (Fig. 7) skeletal muscle using previously modelled resting [Ca²⁺] values.

Discussion

Recent experimental reports implicated hypothetical Ca²⁺ microdomains in paradoxical Ca²⁺-mediated effects on skeletal muscle $Na_v1.4$ activation following pharmacological manoeuvres increasing or decreasing RyR-mediated SR Ca²⁺ release[26,27,30]. They went on to suggest that T-SR junctional sites of close membrane proximity, key to excitation contraction coupling, might form diffusion-restricted, ultrastructurally dispersed intracellular sub-compartments. Although accounting for only a small proportion of total cytosolic volume, these might sustain regulatory local [Ca²⁺] heterogeneities in the vicinity of the tubular $Na_v1.4$[35–37]. These could potentially cause local ~ μM-[Ca²⁺] alterations previously reported to modify Na⁺ channel function[23] arising from direct Ca²⁺, or indirect, Ca²⁺-calmodulin mediated, binding to $Na_v1.4$[18–20,23,24]. Our present modelling studies accordingly explored and characterized conditions required for such Ca²⁺ microdomain formation within these T-SR junctional structures.

The structural parameters describing sarcomere, surface, T-tubular and SR membrane structure, and distributions, densities and electron microscope ultrastructure of their T-SR junctional regions required for such modelling were available for amphibian skeletal muscle[11–13,39–44]. [Ca²⁺] gradients through the resulting formalized geometrical model of a typical T-SR junction in both resting and stimulated muscle fibres were then resolved by finite element method (FEM) solutions of basic Fick diffusion equations. Their boundary conditions first included a RyR-mediated Ca²⁺ release into the T-SR space by a uniform Ca²⁺ influx density J_{influx} across its SR face. Subsequent Ca²⁺ diffusion with a diffusion coefficient established from previous experimental reports from amphibian myoplasm was then mapped through the radially symmetric T-SR junctional space. The second, efflux, boundary condition at the edge of the modelled junction was similarly described by a first order [Ca²⁺]-dependent process into a well-stirred cytosolic space of infinitely large volume. The latter formalism further matched previous reported eventual first order steady state SERCA-mediated resequestration of the released cytosolic Ca²⁺[49].

The boundary conditions simulated conditions both of full and of graded activation by previously reported experimental voltage clamp steps from resting to both 0 mV and varying test potentials and the resulting alterations in cytosolic [Ca²⁺][45]. At the influx boundary, Ca²⁺ influx densities J_{influx} for each voltage were determined directly from the corresponding reported maximum rates of SR Ca²⁺ release, d[Ca²⁺]/dt, and the model geometrical properties. At the efflux boundary, the resulting [Ca²⁺] at the edge of the T-SR junction, [Ca²⁺]$_{edge}$, was first matched to the corresponding experimental maximum cytosolic concentration [Ca²⁺]$_{max}$, by optimising the single free parameter giving exit length $\lambda = 9.2$ nm under conditions of full activation by a test step to 0 mV. This assumed the quantities were proportional and close to each other. Both the latter approximations were then further tested in subsequent explorations of varying J_{influx} through different test voltages. In all events, further corrections for any discrepancies arising from a small [Ca²⁺]$_{edge}$ > [Ca²⁺]$_{max}$ would tend to enhance rather than reduce the computed [Ca²⁺] magnitudes.

The resulting T-SR model predicted Ca²⁺ *microdomains fulfilling the previous suggestions*[30]. The computational solutions following step impositions of J_{influx} converged to give steady state T-SR junctional Ca²⁺ microdomains. Their heatmap representations demonstrated radial [Ca²⁺] gradients extending the entire axial T-SR junction distance. The microdomains were quantified radially at the centre, at distances halfway to, and at the edge of the T-SR junction, in axial regions close to the T-tubular and SR membranes and in the intervening T-SR junction space. Furthermore, varying J_{influx} to reflect previously experimentally reported d[Ca²⁺]/dt, obtained at varying test voltages, at a constant λ value, gave predicted voltage dependences of [Ca²⁺]$_{edge}$ closely approximating those of the corresponding experimental [Ca²⁺]$_{max}$. The accordingly linear, [Ca²⁺]$_{edge}$–[Ca²⁺]$_{max}$ relationship had unity gradient and zero intercept. Furthermore, the [Ca²⁺]$_{edge}$ values themselves depended linearly on the corresponding Ca²⁺ influx Φ_{influx} terms with a gradient fulfilling predictions from the geometrical terms in the equation for the corresponding Ca²⁺ efflux.

All these J_{influx} conditions consistently generated T-SR junction Ca²⁺ microdomains containing physiologically significant, ~ μM-[Ca²⁺], heterogeneities graded with imposed depolarization. These could locally elevate [Ca²⁺] from ~ 0.3–0.4 μM at activation threshold, to 17–20 μM at full activation, relative to the remaining bulk

extra-junctional cytosolic [Ca^{2+}]. These microdomains all extended through the entire axial T-SR distance. They showed similar normalised [Ca^{2+}] profiles with radial distance, in which [Ca^{2+}] declined > fivefold from its maximum in the centre to the edge of the T-SR junction. The spatial [Ca^{2+}] dependences persisted with proportionately reduced [Ca^{2+}] even with 10 and 100-fold J_{influx} reductions below threshold levels for observed Ca^{2+} release[45]. These modelling studies adopting established quantifications for baseline T-SR and sarcomere membrane structure, and diffusion coefficient values, D could thus replicate reported physiological d[Ca^{2+}]/dt and [Ca^{2+}]$_{max}$ in activated amphibian skeletal muscle.

Detailed characteristics of such membrane appositions vary amongst muscle or cell types, and with physiological and physical conditions. Nevertheless, *microdomain formation and characteristics were robust through systematic tests at constant J_{influx} that varied Ca^{2+} diffusion coefficient, D, T-SR distance, w, and T-SR diameter, d, in turn, holding the remaining variables constant.* These tests further made it possible to survey the relative importance of diffusional or geometric properties to microdomain formation and characteristics.

First, alterations in D within the T-SR space could reflect Ca^{2+} buffering capacities, $\kappa = (\Delta[\text{bound Ca}]/\Delta[\text{free Ca}])$, of its contained immobile and mobile buffers, and the diffusion coefficient D_{mobile} of the mobile buffer. Assuming the rapid buffer approximation, the resulting steady state D is related to the free diffusion coefficient D_{Ca2+} by the expression[65–67]:

$$D_{Ca2+}\left\{1 + \frac{D_{mobile}}{D_{Ca2+}}\right\}\kappa_{mobile}/\{1 + \kappa_{mobile} + \kappa_{immobile}\}$$

Immobile buffer could reflect fixed Ca^{2+} binding sites including negatively charged membrane bilayer phospholipid groups[68] and Ca^{2+}-binding domains in Ca^{2+} dependent ion channel, cytoskeletal, transport motor and membrane-associated Ca^{2+} binding kinase proteins[69]. This would generate local, steady state equilibria between Ca^{2+} binding and Ca^{2+} diffusion: depleted Ca^{2+}-free immobile buffer cannot be replaced by diffusion from remote sites. Immobile buffer would then leave steady-state Ca^{2+} microdomains unaffected[67]. Whilst its action could alter the [Ca^{2+}] kinetics, our modelled step impositions of Ca^{2+} influxes increased T-SR free [Ca^{2+}] to steady state values over ~ 0.2 ms exponential timecourses. These were 1–2 orders of magnitude shorter than those of experimentally observed Ca^{2+} transients[45,70]. In contrast, *mobile buffer* could influence D to extents dependent upon κ_{mobile} and D_{mobile}. Our computations explored a wide range of conditions extending from limiting maximal D values at infinite Ca^{2+} dilution without buffer[55] then progressively reducing D to values yielding T-SR [Ca^{2+}] values approaching and exceeding SR [Ca^{2+}]. They included physiologically realistic values corresponding to known in vivo Ca^{2+} buffering capacities of ~50 and ~100 in the respective absence and presence of 1 mM MgATP[51,71], and empirical in vivo skeletal muscle values[46–48].

These explorations demonstrated persistent [Ca^{2+}] heterogeneities despite large increases or decreases in diffusion coefficient D relative to established skeletal myocyte cytosolic values ($D = 4.0 \times 10^7$ nm^2/s)[46–48], including values reported either in vitro[55,56] or in other cell types[50–54]. On the one hand, even the highest reported, in vitro, $D = 1 \times 10^9$ nm^2/s, value corresponding to infinite dilution[55] persistently yielded [Ca^{2+}] microdomains approaching μM-[Ca^{2+}] at the T-SR junction centre. On the other, the electron-densities within T-SR junctions could reflect local protein, lipid or ion concentrations reducing D[44]. Here, progressive tenfold decreases down to $D = 4.0 \times 10^5$ nm^2/s predicted ~ mM hypothetical [Ca^{2+}] actually approaching reported in situ free SR [Ca^{2+}] (~ 3.6 mM; assuming a 6.1 mM SR [calsequestrin] with a 1.1 mM Ca^{2+} binding constant[57]). These correspondingly slowed the formation time courses of such microdomains. Nevertheless, in the steady state, through this entire explored D range, Ca^{2+} microdomains persisted with unchanged radial [Ca^{2+}] profiles extending the full distance between T and SR membranes confirming the linearity condition in this model system. [Ca^{2+}]$_{edge}$ varied inversely with D, giving a dependence and proportionality constant that matched predictions of the T-SR junctional model.

Secondly, whilst averaging $w = 12$ nm in resting muscle, axial T-SR distances range from 6 nm with increased extracellular tonicity[58] to 20 nm with fatiguing stimulation[59,60]. Varying w through this range here disrupted microdomain characteristics resulting in heatmaps showing tapering plume-like appearances at the largest T-SR distances. There were increased radial [Ca^{2+}] nonuniformities themselves varying along the axial distance between SR and T-tubular membranes, to extents increasing with increasing w. Nevertheless, [Ca^{2+}]$_{edge}$ varied with w, through an inverse relationship with proportionality constant matching predictions of the T-SR junction model. Thirdly, successive reductions of T-SR junctional diameters, from $d = 220$ nm to $d = 40$ nm, similarly disrupted Ca^{2+} microdomain heatmaps again giving tapering plume-like forms at the smallest diameters. These were quantified as increased radial non-uniformities and marked axial [Ca^{2+}] differences between regions close to the SR and T-tubular membranes and the intervening space along the axial T-SR distance. Falls in [Ca^{2+}] with radial distance from the T-SR junction centre and [Ca^{2+}] at the SR relative to the T-tubular membranes became less marked with decreasing d. Finally [Ca^{2+}]$_{edge}$ increased with d as expected from the T-SR junction model. Nevertheless, through both these latter modifications in T-SR junction geometry, despite their altered spatial characteristics, the ~ μM-[Ca^{2+}] heterogeneities between their periphery and centre persisted even with more than 100% increases in T-SR distance or 75% reductions in T-SR diameter from control values derived from established morphometric data.

The previous experimental reports had also invoked background, RyR-mediated influxes of Ca^{2+} in Ca^{2+} microdomain generation in resting in addition to activated muscle[27,30]. Accordingly, *the T-SR junction model was extended further to investigate formation and properties of Ca^{2+} microdomains in resting myocytes.* This employed background J_{influx} values calculated from previously reported cytosolic [Ca^{2+}] values in resting muscle. These previous Fura-red fluorescence studies had suggested experimental resting [Ca^{2+}] ranging between 0.060 to 0.140 μmol/dm^3 (ref. [61]). We further explored further reduced resting [Ca^{2+}] limits of ~ 0.038 μmol/dm^3 from Ca^{2+}-sensitive microelectrode studies[64] and possible higher 0.300 μmol/dm^3 limits[62,63]. The resulting T-SR modelling continued to predict Ca^{2+} microdomains with their characteristic spatial characteristics. Furthermore,

microdomain [Ca^{2+}] levels at the T-SR centre, whether close to the T-tubular or SR membranes or in the intervening space, approached or attained ~ μM-[Ca^{2+}].

The present findings taken together could be used to reconstruct the proportions of T-tubular membrane area and therefore of resident Na$_v$1.4 exposed to successively greater levels of T-SR junction microdomain [Ca^{2+}] in both activated and resting muscle. Successively greater proportions of activated T-tubular membrane became exposed to successively higher, 0.1 to 10 μM [Ca^{2+}] with increasing depolarization. In addition, significant proportions of even resting T-tubular membrane remained exposed to significant, ~ 0.5 μM [Ca^{2+}]. These findings therefore provide a physical basis for the previous suggestions implicating Ca^{2+} microdomain formation in observed modifications in Na$_v$1.4 function[27,30]. Ca^{2+}-CaM binding takes place with ~ μM [Ca^{2+}] dissociation constants[72,73]. Feedback μM-[Ca^{2+}] levels arising from SR Ca^{2+} release could therefore potentially modify both skeletal[26,27,30] and cardiac muscle[28,29] Na$_v$1.4 or Na$_v$1.5 through direct or indirect, Ca^{2+}-calmodulin (Ca^{2+}-CaM) mediated, actions on their C-terminal domains[16,18–20,23,24]. Such concentrations further match the photorelease-induced 1–2 μM cytosolic [Ca^{2+}] elevations previously reported to modify Na$_v$1.4 function[23].

In skeletal muscle, elevated T-SR junctional microdomain [Ca^{2+}] could inhibit tubular Na$_v$1.4 function following normal sustained activity[59,60] and contribute to particular clinical skeletal myopathies[74]. A myotonic hyperexcitability disorder disrupting Ca^{2+}-mediated inhibition of Na$_v$1.4 function has been associated with Na$_v$1.4 C-terminal EF hand-like domain mutations[75,76]. A condition associated with increased myotube diameters and resting [Ca^{2+}]$_i$, and decreased RyR1-mediated Ca^{2+} release reflecting possible abnormalities in triad junction formation and maintenance is associated with another, junctophilin (JP2), mutation[77]. In murine cardiac muscle, Na$_v$1.5 inhibition followed increased SR Ca^{2+} release following pharmacological challenge[28,29] and in RyR2-P2328S variants modelling the pro-arrhythmogenic catecholaminergic polymorphic ventricular tachycardia[78–80]. In these examples, the underlying in vivo source of microdomain Ca^{2+} would likely remain the RyR-mediated Ca^{2+} release modelled here, as opposed to T-tubular Ca$_v$1.1 or Ca$_v$1.2 channel mediated entry of extracellular Ca^{2+}. Thus, early Ca^{2+} skeletal muscle voltage clamp currents, I_{Caf} (~ 25 μA/cm^2)[81] and later cell attached patch clamped cardiomyocyte I_{CaL} (~ 10 pA/pF[82]; would contribute J_{influx} terms (~ 8.64 × 10^{-7} and ~ 6.91 × 10^{-8} mol/m^2/s assuming similar C_T/C_S and ξ; respectively) one and two orders of magnitude lower than the corresponding RyR-mediated J_{influx}, at comparable test voltages. The larger skeletal muscle late I_{Ca} (80 μA/cm2, giving J_{influx} ~ 2.76 × 10^{-6} mol/m^2/s) evolves over time courses (hundreds of ms) more prolonged than excitation contraction coupling and shows rapid off kinetics on action potential repolarization[83,84].

Microdomain μM-[Ca^{2+}] could also regulate other signalling biomolecules. They are involved in a bell-shaped in vitro open probability relationship for single channel RyR activation and inhibition[14]. Here, cardiac and neuronal, RyR2 and RyR3 are more Ca^{2+}-sensitive than RyR1 but all are activated over the ~ 1 μM [Ca^{2+}] predicted in the present analysis[85,86]. However, under their respective in vivo physiological [ATP] and [Mg^{2+}] conditions, cardiac[87] but not skeletal muscle[88] RyR activation involves Ca^{2+}-induced Ca^{2+} release. Skeletal muscle RyR activation instead involves direct allosteric coupling with either T-tubular Ca$_v$1.1-L-type Ca^{2+} channel voltage sensors[15] or possibly other adjacent SR RyRs themselves coupled to such Ca$_v$1.1[89,90]. ~ μM Ca^{2+}-CaM may also exert other cytosolic effects as on glyceraldehyde 3-phosphate dehydrogenase[91] or itself provide local signaling domains[36].

Closely apposed membranes potentially mediating localized Ca^{2+} signalling involving Ca^{2+}-dependent proteins that would similarly permit divergent signalling at different sites also occur in widespread other cell types[9,10]. At smooth muscle SR-plasma membrane appositions[92], local Ca^{2+} could modulate repolarizing Ca^{2+}-activated K$^+$ channel activity[93]. They also occur in neurons[6]; cerebellar Purkinje and hippocampal neurones similarly signal using RyR- Ca^{2+} release channels[1–4]. Amongst non-excitable cells, multiple 20–30 nm diameter membrane invaginations in thrombocyte open canalicular systems (OCS)[7,8] form vacuolar structures apposed to membranes of the Ca^{2+}-storing deep tubular system (DTS) previously compared with muscle T-SR junctions[94]. These gate inositol trisphosphate receptor rather than RyR mediated Ca^{2+} fluxes into the junction upon agonist stimulation. The theoretical analysis here thus combined available experimental anatomical and physiological data and diffusion theory to predict significant [Ca^{2+}] heterogeneities in the skeletal muscle T-SR-junction. Its findings might next prompt investigations of structure and function in these further examples. These might be complemented by direct experimental fluorescent Ca^{2+} indicator [Ca^{2+}]$_{TSR}$ measurements[35–37] were these to be able to address the small dimensions and dispersed nature of the microcompartments concerned.

Materials and methods

Finite element analysis.   Diffusional mechanics and its consequent temporal and spatial [Ca^{2+}] patterns were computationally examined in a model T-SR junction. This involved replicating the geometry within and through which the diffusional processes occurred, pre-processing through meshing and definition of physical conditions including loads, initial and boundary conditions, generation of system solutions and post-processing of the results (Supplementary Fig. S1). The matrix-based programming platform and language MATLAB (version R2020b win64 9.9.0.1467703, version released August 26th, 2020, MathWorks, Cambridge, UK) performed the required data array manipulations and generated all the graphics in Figs. 1, 2, 3, 4, 5, 6, 7, and 8 (https://www.mathworks.com/discovery/what-is-matlab.html). It was implemented on an IBM compatible computer (CPU: Intel Core; i7-4790 K CPU: 4.40 GHz (4 cores); GPU: ASUS STRIX GeForce GTX970; installed RAM: 16 GB, running Windows (Microsoft, Washington, USA) 10, Home 64-bit version 1909).

The underlying T-SR junction geometry was reconstructed virtually for use in a finite element analysis solving partial differential equations (PDEs) for the resulting diffusional processes with their accompanying boundary conditions (BCs) (See Supplementary File for software archive). The finite element method (FEM) described the complex geometry as a collection of subdomains (elements) by superimposing upon this geometry a mesh of tetrahedral elements joined at their vertices (nodes) and edges. The subdivision accurately represents this complex

geometry, permits inclusion of dissimilar material properties, and provides a straightforward representation of the total solution whilst capturing local, microdomain, effects.

Boundary conditions and equation solutions. Specified BCs provided values of the field and related variables, in the present case, the normal derivatives of the field variable in the form of a Neumann-type BC. The FEM equations are formulated such that at the nodal connections, the value of the field variable at any connection is the same for each element connected to the node. Solutions at the edges of each adjacent element are therefore equal, ensuring continuity of field variables between elements, avoiding physically unacceptable gaps or voids in the solution[38]. The original PDE problem is accordingly represented within each element with simpler equations approximating the solution to the original equations. Stationary linear problems whose coefficients are independent of the solution or its gradient yield a linear system of equations. In this case our PDE is time-dependent and hence the system of simpler equations is a set of ordinary differential equations (ODEs) then passed onto MATLAB solvers for numerical integration for solution. The FEM approximates the solution by minimizing the associated error function, automatically finding the linear combination of basis functions closest to the solution u. The FEM could therefore capture both concentration differences local to the T-tubular and SR membranes, and across the entire modelled geometry.

Partial differential equation toolbox™. Meshing and application of the FEM used Partial Differential Equation Toolbox (version 3.5 installed on 8th October 2020 by MathWorks) within MATLAB. This provides functions for solving structural mechanics, heat transfer and general PDEs using the FEM (https://www.mathworks.com/products/pde.html). PDE Toolbox also provides the ability to automatically mesh the T-SR junction geometry, providing a basis for solving the diffusion PDE, and stores the solution as matrices amenable to various methods of presentation and post-processing of data within MATLAB. The PDE toolbox is designed to solve equations of the form:

$$m\frac{\mathrm{d}^2 u}{\mathrm{d}t^2} + b\frac{\mathrm{d}u}{\mathrm{d}t} - \nabla \cdot (c\nabla u) + hu = f \tag{17}$$

with a generalised Neumann boundary condition of:

$$\overrightarrow{n} \cdot (c\nabla u) + qu = g \tag{18}$$

where the coefficients m, b, h, f and g can be functions of spatial position, the solution u, or its spatial gradient. In a diffusive system, this generalised problem reduces to the first order equation:

$$b\frac{\partial u}{\partial t} - \nabla \cdot (c\nabla u) + hu = f \tag{19}$$

with b set to unity, where c represents the diffusion coefficient D, and h represents the boundary flux term for the Neumann condition (compare Eq. 4).

Ethical approval. This entirely theoretical study did not involve animal procedures.

Data availability
The data that support the findings of this study are available from the corresponding author upon reasonable request and are furthermore summarized in the Supplementary file.

References
1. Kano, M., Garaschuk, O., Verkhratsky, A. & Konnerth, A. Ryanodine receptor-mediated intracellular calcium release in rat cerebellar Purkinje neurones. *J. Physiol.* **487**, 1–16 (1995).
2. Kohda, K., Inoue, T. & Mikoshiba, K. Ca2+ release from Ca2+ stores, particularly from ryanodine-sensitive Ca2+ stores, is required for the induction of LTD in cultured cerebellar Purkinje cells. *J. Neurophysiol.* **74**, 2184–2188 (1995).
3. Ouyang, Y. *et al.* Differential distribution and subcellular localization of ryanodine receptor isoforms in the chicken cerebellum during development. *Brain Res.* **775**, 52–62 (1997).
4. Tedoldi, A. *et al.* Calcium-induced calcium release and type 3 ryanodine receptors modulate the slow afterhyperpolarising current, sIAHP, and its potentiation in hippocampal pyramidal neurons. *PLoS ONE* **15**, 1316 (2020).
5. Sharp, A. H. *et al.* Differential immunohistochemical localization of inositol 1,4,5- trisphosphate- and ryanodine-sensitive Ca2+ release channels in rat brain. *J. Neurosci.* **13**, 3051–3063 (1993).
6. Wu, Y. *et al.* Contacts between the endoplasmic reticulum and other membranes in neurons. *Proc. Natl. Acad. Sci. USA* **114**, E4859–E4867 (2017).
7. Sage, S. O., Pugh, N., Farndale, R. W. & Harper, A. G. S. Pericellular Ca2+ recycling potentiates thrombin-evoked Ca2+ signals in human platelets. *Physiol. Rep.* **1**, 5 (2013).
8. Anand, P. & Harper, A. G. S. Human platelets use a cytosolic Ca2+ nanodomain to activate Ca2+-dependent shape change independently of platelet aggregation. *Cell Calcium* **90**, 102248 (2020).
9. Chang, C. L., Chen, Y. J. & Liou, J. ER-plasma membrane junctions: Why and how do we study them?. *Biochim. Biophys. Acta Mol. Cell Res.* **1864**, 1494–1506 (2017).
10. Henkart, M., Landis, D. M. D. & Reese, T. S. Similarity of junctions between plasma membranes and endoplasmic reticulum in muscle and neurons. *J. Cell Biol.* **70**, 338–347 (1976).

11. Franzini-Armstrong, C., Protasi, F. & Ramesh, V. Shape, size, and distribution of Ca²⁺ release units and couplons in skeletal and cardiac muscles. *Biophys. J.* **77**, 1528–1539 (1999).
12. Franzini-Armstrong, C. & Nunzi, G. Junctional feet and particles in the triads of a fast-twitch muscle fibre. *J. Muscle Res. Cell Motil.* **4**, 233–252 (1983).
13. Kelly, D. E. The fine structure of skeletal muscle triad junctions. *J. Ultrastruct. Res.* **29**, 37–49 (1969).
14. Endo, M. Calcium-induced calcium release in skeletal muscle. *Physiol. Rev.* **89**, 1153–1176 (2009).
15. Huang, C.L.-H., Pedersen, T. H. & Fraser, J. A. Reciprocal dihydropyridine and ryanodine receptor interactions in skeletal muscle activation. *J. Muscle Res. Cell Motil.* **32**, 171–202 (2011).
16. Nathan, S. *et al.* Structural basis of cytoplasmic NaV1.5 and NaV1.4 regulation. *J. Gen. Physiol.* **153**, 1–10 (2021).
17. Yoder, J. B. *et al.* Ca²⁺-dependent regulation of sodium channels NaV1.4 and NaV1.5 is controlled by the post-IQ motif. *Nat. Commun.* **10**, 1514. https://doi.org/10.1038/s41467-019-09570-7 (2019).
18. Gardill, B. R., Rivera-Acevedo, R. E., Tung, C. C. & Van Petegem, F. Crystal structures of Ca²⁺–calmodulin bound to NaV C-terminal regions suggest role for EF-hand domain in binding and inactivation. *Proc. Natl. Acad. Sci. USA.* **166**, 10763–10772 (2019).
19. Young, K. A. & Caldwell, J. H. Modulation of skeletal and cardiac voltage-gated sodium channels by calmodulin. *J. Physiol.* **565**, 349–370 (2005).
20. Potet, F. *et al.* Functional Interactions between distinct sodium channel cytoplasmic domains through the action of calmodulin. *J. Biol. Chem.* **284**, 8846–8854 (2009).
21. Loussouarn, G. *et al.* Physiological and pathophysiological insights of Nav1.4 and Nav1.5 comparison. *Front. Pharmacol.* **6**, 314. https://doi.org/10.3389/fphar.2015.00314 (2016).
22. Bendahhou, S., Cummins, T. R., Potts, J. F., Tong, J. & Agnew, W. S. Serine-1321-independent regulation of the mu 1 adult skeletal muscle Na⁺ channel by protein kinase C. *Proc. Natl. Acad. Sci. USA.* **92**, 12003–12007 (1995).
23. Ben-Johny, M. *et al.* Conservation of Ca²⁺/Calmodulin Regulation across Na and Ca²⁺ channels. *Cell* **157**, 1657–1670 (2014).
24. Deschênes, I. *et al.* Isoform-specific modulation of voltage-gated Na⁺ channels by calmodulin. *Circ. Res.* **90**, e49–e57 (2002).
25. Almers, W., Stanfield, P. R. & Stühmer, W. Lateral distribution of sodium and potassium channels in frog skeletal muscle: Measurements with a patch-clamp technique. *J. Physiol.* **336**, 261–284 (1983).
26. Matthews, H. R. *et al.* Sodium current inhibition following stimulation of exchange protein directly activated by cyclic-3′,5′-adenosine monophosphate (Epac) in murine skeletal muscle. *Sci. Rep.* **9**, 1927 (2019).
27. Sarbjit-Singh, S., Matthews, H. R. & Huang, C. L.-H. Ryanodine receptor modulation by caffeine challenge modifies Na⁺ current properties in intact murine skeletal muscle fibres. *Sci. Rep.* **10**, 2199 (2020).
28. Valli, H. *et al.* Epac-induced ryanodine receptor type 2 activation inhibits sodium currents in atrial and ventricular murine cardiomyocytes. *Clin. Exp. Pharmacol. Physiol.* **45**, 278–292 (2018).
29. King, J. *et al.* Loss of Nav1.5 expression and function in murine atria containing the RyR2-P2328S gain-of-function mutation. *Cardiovasc. Res.* **99**, 751–759 (2013).
30. Liu, S. X., Matthews, H. R. & Huang, C.L.-H. Sarcoplasmic reticular Ca²⁺-ATPase inhibition paradoxically upregulates murine skeletal muscle Nav14 function. *Sci. Rep.* **11**, 84593 (2021).
31. Du, G. G., Ashley, C. C. & Lea, T. J. Effects of thapsigargin and cyclopiazonic acid on the sarcoplasmic reticulum Ca²⁺ pump of skinned fibres from frog skeletal muscle. *Pflügers Arch.* **429**, 169–175 (1994).
32. Seidler, N. W., Jona, I., Vegh, M. & Martonosi, A. Cyclopiazonic acid is a specific inhibitor of the Ca²⁺-ATPase of sarcoplasmic reticulum. *J. Biol. Chem.* **264**, 17816–17823 (1989).
33. Pagala, M. K. D. & Taylor, S. R. Imaging caffeine-induced Ca²⁺ transients in individual fast-twitch and slow-twitch rat skeletal muscle fibers. *Am. J. Physiol. Physiol.* **274**, C623–C632 (1998).
34. Sekiguchi, F. *et al.* Effects of cyclopiazonic acid on contraction and intracellular Ca²⁺ in oesophageal striated muscle of normotensive and spontaneously hypertensive rats. *Br. J. Pharmacol.* **128**, 961–968 (1999).
35. Despa, S. *et al.* Junctional cleft [Ca²⁺]ᵢ measurements using novel cleft-targeted Ca²⁺ sensors. *Circ. Res.* **115**, 339–347 (2014).
36. Saucerman, J. J. & Bers, D. M. Calmodulin binding proteins provide domains of local Ca²⁺ signaling in cardiac myocytes. *J. Mol. Cell. Cardiol.* **52**, 312–316 (2012).
37. Sanchez, C. *et al.* Detection of Ca²⁺ transients near ryanodine receptors by targeting fluorescent Ca²⁺sensors to the triad. *J. Gen. Physiol.* **153**, e202012592. doi: 10.1085/jgp.202012592.(2021).
38. Reddy, J. N. *An Introduction to The Finite Element Method* 3rd edn. (McGraw-Hill, 2005).
39. Adrian, R. H. & Peachey, L. D. Reconstruction of the action potential of frog sartorius muscle. *J. Physiol.* **235**, 103–131 (1973).
40. Falk, G. & Fatt, P. Linear electrical properties of striated muscle fibres observed with intracellular microelectrodes. *Proc. R. Soc. Lond. Ser. B.* **160**, 69–123 (1964).
41. Gordon, A. M., Huxley, A. F. & Julian, F. J. The variation in isometric tension with sarcomere length in vertebrate muscle fibres. *J. Physiol.* **184**, 170–192 (1966).
42. Dulhunty, A. F. Excitation-contraction coupling from the 1950s into the new millennium. *Clin. Exp. Pharmacol. Physiol.* **33**, 763–772 (2006).
43. Franzini-Armstrong, C. Studies of the triad: IV. Structure of the junction in frog slow fibers. *J. Cell Biol.* **56**, 120–128 (1973).
44. Franzini-Armstrong, C. Studies of the triad: I. Structure of the junction in frog twitch fibers. *J. Cell Biol.* **47**, 488–499 (1970).
45. Kovacs, L., Rios, E. & Schneider, M. F. Measurement and modification of free calcium transients in frog skeletal muscle fibres by a metallochromic indicator dye. *J. Physiol.* **343**, 161–196 (1983).
46. Baylor, S. M. & Hollingworth, S. Model of sarcomeric Ca²⁺ movements, including ATP Ca²⁺ binding and diffusion, during activation of frog skeletal muscle. *J. Gen. Physiol.* **112**, 297–316 (1998).
47. Baylor, S. M., Hollingworth, S. & Chandler, W. K. Comparison of simulated and measured calcium sparks in intact skeletal muscle fibers of the frog. *J. Gen. Physiol.* **120**, 349–368 (2002).
48. Kushmerick, M. J. & Podolsky, R. J. Ionic mobility in muscle cells. *Science* **166**, 1297–1298 (1969).
49. Melzer, W., Ríos, E. & Schneider, M. F. The removal of myoplasmic free calcium following calcium release in frog skeletal muscle. *J. Physiol.* **372**, 261–292 (1986).
50. Donahue, B. S. & Abercrombie, R. F. Free diffusion coefficient of ionic calcium in cytoplasm. *Cell Calcium* **8**, 437–448 (1987).
51. Al-Baldawi, N. F. & Abercrombie, R. F. Calcium diffusion coefficient in *Myxicola* axoplasm. *Cell Calcium* **17**, 422–430 (1995).
52. Cordeiro, J. M. *et al.* Location of the initiation site of calcium transients and sparks in rabbit heart Purkinje cells. *J. Physiol.* **531**, 301–314 (2001).
53. Nasi, E. & Tillotson, D. The rate of diffusion of Ca²⁺ and Ba²⁺ in a nerve cell body. *Biophys. J.* **47**, 735–738 (1985).
54. Swietach, P., Spitzer, K. W. & Vaughan-Jones, R. D. Modeling calcium waves in cardiac myocytes: Importance of calcium diffusion. *Front. Biosci.* **15**, 661–680 (2010).
55. Vanýsek, P. Ionic conductivity and diffusion at infinite dilution. In: Handbook of chemistry and physics. *CRC Handb. Chem. Physics, Ed. 91* **96**, 5–98 (2002).
56. Wang, J. H. Tracer-diffusion in liquids. IV. Self-diffusion of calcium ion and chloride ion in aqueous calcium chloride solutions. *J. Am. Chem. Soc.* **75**, 1769–1770 (1953).
57. Volpe, P. & Simon, B. J. The bulk of Ca²⁺ released to the myoplasm is free in the sarcoplasmic reticulum and does not unbind from calsequestrin. *FEBS Lett.* **278**, 274–278 (1991).

58. Chawla, S., Skepper, J. N., Hockaday, A. R. & Huang, C. L.-H. Calcium waves induced by hypertonic solutions in intact frog skeletal muscle fibres. *J. Physiol.* **536**, 351–359 (2001).
59. Usher-Smith, J. A., Fraser, J. A., Huang, C.L.-H. & Skepper, J. N. Alterations in triad ultrastructure following repetitive stimulation and intracellular changes associated with exercise in amphibian skeletal muscle. *J. Muscle Res. Cell Motil.* **28**, 19–28 (2007).
60. Martin, C. A. *et al.* The effect of extracellular tonicity on the anatomy of triad complexes in amphibian skeletal muscle. *J. Muscle Res. Cell Motil.* **24**, 407–415 (2003).
61. Konishi, M. & Watanabe, M. Resting cytoplasmic free Ca^{2+} concentration in frog skeletal muscle measured with fura-2 conjugated to high molecular weight dextran. *J. Gen. Physiol.* **106**, 1123–1150 (1995).
62. Harkins, A. B., Kurebayashi, N. & Baylor, S. M. Resting myoplasmic free calcium in frog skeletal muscle fibers estimated with fluo-3. *Biophys. J.* **65**, 865–881 (1993).
63. Kurebayashi, N., Harkins, A. B. & Baylor, S. M. Use of fura red as an intracellular calcium indicator in frog skeletal muscle fibers. *Biophys. J.* **64**, 1934–1960 (1993).
64. Blatter, L. A. & Blinks, J. R. Simultaneous measurement of Ca^{2+} in muscle with Ca electrodes and aequorin: Diffusible cytoplasmic constituent reduces Ca^{2+}-independent luminescence of aequorin. *J. Gen. Physiol.* **98**, 1141–1160 (1991).
65. Wagner, J. & Keizer, J. Effects of rapid buffers on Ca^{2+} diffusion and Ca^{2+} oscillations. *Biophys. J.* **67**, 447–456 (1994).
66. Zador, A. & Koch, C. Linearized models of calcium dynamics: Formal equivalence to the cable equation. *J. Neurosci.* **14**, 4705–4715 (1994).
67. Matthews, E. A. & Dietrich, D. Buffer mobility and the regulation of neuronal calcium domains. *Front. Cell. Neurosci.* **9**, 48 (2015).
68. McLaughlin, S., Mulrine, N., Gresalfi, T., Vaio, G. & McLaughlin, A. Adsorption of divalent cations to bilayer membranes containing phosphatidylserine. *J. Gen. Physiol.* **77**, 445–473 (1981).
69. Schwaller, B. Cytosolic Ca^{2+} buffers. *Cold Spring Harb. Perspect. Biol.* **2**, a004051. https://doi.org/10.1101/cshperspect.a004051 (2010).
70. Naraghi, M. & Neher, E. Linearized buffered Ca^{2+} diffusion in microdomains and its implications for calculation of $[Ca^{2+}]$ at the mouth of a calcium channel. *J. Neurosci.* **17**, 6961–6973 (1997).
71. Al-Baldawi, N. F. & Abercrombie, R. F. Cytoplasmic calcium buffer capacity determined with Nitr-5 and DM-nitrophen. *Cell Calcium* **17**, 409–421 (1995).
72. Stefan, M. I., Edelstein, S. J. & Le Novère, N. An allosteric model of calmodulin explains differential activation of PP2B and CaMKII. *Proc. Natl. Acad. Sci. USA.* **105**, 10768–10773 (2008).
73. Lai, M., Brun, D., Edelstein, S. J. & Le Novère, N. Modulation of calmodulin lobes by different targets: An allosteric model with hemiconcerted conformational transitions. *PLoS Comput. Biol.* **11**, e1004093 (2015).
74. Dowling, J. J., Lawlor, M. W. & Dirksen, R. T. Triadopathies: An emerging class of skeletal muscle diseases. *Neurotherapeutics* **11**, 773–785 (2014).
75. Biswas, S., DiSilvestre, D. A., Dong, P. & Tomaselli, G. F. Mechanisms of a human skeletal myotonia produced by mutation in the C-terminus of NaV1.4: Is Ca^{2+} regulation defective?. *PLoS ONE* **8**, e08163 (2013).
76. Horie, R. *et al.* EF hand-like motif mutations of Nav1.4 C-terminus cause myotonic syndrome by impairing fast inactivation. *Muscle Nerve* https://doi.org/10.1002/mus.26849 (2020).
77. Woo, J. S. *et al.* S165F mutation of junctophilin 2 affects Ca^{2+} signalling in skeletal muscle. *Biochem. J.* **427**, 125–134 (2010).
78. Huang, C.L.-H. Murine electrophysiological models of cardiac arrhythmogenesis. *Physiol. Rev.* **97**, 283–409 (2017).
79. Zhang, Y. *et al.* Acute atrial arrhythmogenicity and altered Ca^{2+} homeostasis in murine RyR2-P2328S hearts. *Cardiovasc. Res.* **89**, 794–804 (2011).
80. Zhang, Y. *et al.* Conduction slowing contributes to spontaneous ventricular arrhythmias in intrinsically active murine RyR2-P2328S hearts. *J. Cardiovasc. Electrophysiol.* **24**, 210–218 (2013).
81. Cota, G. & Stefani, E. A fast-activated inward calcium current in twitch muscle fibres of the frog (*Rana montezume*). *J. Physiol.* **370**, 151–163 (1986).
82. Morinaga, A., Ito, J., Niimi, T. & Maturana, A. D. RBM20 regulates CaV1.2 surface expression by promoting exon 9* Inclusion of CACNA1C in neonatal rat cardiomyocytes. *Int. J. Mol. Sci.* **20**, 5591 (2019).
83. Sanchez, J. A. & Stefani, E. Inward calcium current in twitch muscle fibres of the frog. *J. Physiol.* **283**, 197–209 (1978).
84. Sánchez, J. A. & Stefani, E. Kinetic properties of calcium channels of twitch muscle fibres of the frog. *J. Physiol.* **337**, 1–17 (1983).
85. Percival, A. L. *et al.* Chicken skeletal muscle ryanodine receptor isoforms: ion channel properties. *Biophys. J.* **67**, 1834–1850 (1994).
86. Murayama, T. & Ogawa, Y. RyR1 exhibits lower gain of CICR activity than RyR3 in the SR: Evidence for selective stabilization of RyR1 channel. *Am. J. Physiol. Cell Physiol.* **287**, 12 (2004).
87. Fabiato, A. & Fabiato, F. Contractions induced by a calcium-triggered release of calcium from the sarcoplasmic reticulum of single skinned cardiac cells. *J. Physiol.* **249**, 469–495 (1975).
88. Figueroa, L. *et al.* Synthetic localized calcium transients directly probe signalling mechanisms in skeletal muscle. *J. Physiol.* **590**, 1389–1411 (2012).
89. Marx, S. O., Ondrias, K. & Marks, A. R. Coupled gating between individual skeletal muscle Ca^{2+} release channels (ryanodine receptors). *Science* **281**, 818–821 (1998).
90. Huang, C.L.-H. Charge movements in intact amphibian skeletal muscle fibres in the presence of cardiac glycosides. *J. Physiol.* **532**, 509–523 (2001).
91. Singh, P., Salih, M., Leddy, J. J. & Tuana, B. S. The muscle-specific calmodulin-dependent protein kinase assembles with the glycolytic enzyme complex at the sarcoplasmic reticulum and modulates the activity of glyceraldehyde-3-phosphate dehydrogenase in a Ca^{2+}/ calmodulin-dependent manner. *J. Biol. Chem.* **279**, 35176–35182 (2004).
92. Devine, C. E., Somlyo, A. V. & Somlyo, A. P. Sarcoplasmic reticulum and excitation-contraction coupling in mammalian smooth muscles. *J. Cell Biol.* **52**, 690–718 (1972).
93. Knot, H. J., Standen, N. B. & Nelson, M. T. Ryanodine receptors regulate arterial diameter and wall $[Ca^{2+}]$ in cerebral arteries of rat via Ca^{2+}-dependent K^+ channels. *J. Physiol.* **508**, 211–221 (1998).
94. Van Nispen Tot Pannerden, H. *et al.* The platelet interior revisited: Electron tomography reveals tubular α-granule subtypes. *Blood* **116**, 1147–1156 (2010).

Acknowledgements

Author contributions

H.R.M. introduced use of the MATLAB system. C.L.-H.H. parametrized the T-SR model. O.J.B. developed, iterated, and ran the programmes including generating the graphical output. H.R.M. and C.L.-H.H. supervised project execution. C.L.-H.H. conceived the project and wrote the paper in conjunction with O.J.B and H.R.M.

Competing interests

The authors declare no competing interests.

Additional information

Supplementary Information The online version contains supplementary material available at https://doi.org/10.1038/s41598-021-93083-1.

Correspondence and requests for materials should be addressed to C.L.-H.H.

Reprints and permissions information is available at www.nature.com/reprints.

Publisher's note Springer Nature remains neutral with regard to jurisdictional claims in published maps and institutional affiliations.